



Available online at www.sciencedirect.com

ScienceDirect

Advances in Space Research 63 (2019) 476–495

**ADVANCES IN
SPACE
RESEARCH**
(*a COSPAR publication*)
www.elsevier.com/locate/asr

Dynamics in the Phobos environment

D.J. Scheeres ^{*}, S. Van wal, Z. Olikara ¹, N. Baresi ²

Smead Department of Aerospace Engineering Sciences, The University of Colorado Boulder, United States

Received 22 March 2018; received in revised form 8 October 2018; accepted 11 October 2018

Available online 23 October 2018

Abstract

The dynamical environment on and about the Martian moon Phobos is explored. This planetary moon provides a unique dynamical environment in the solar system, being subject to extreme tidal forces and having a characteristically non-spherical shape. Further, it is not in a fully circular orbit, meaning that it has librations that arise from its eccentricity, contributing to a periodic forcing environment. Thus, to plan and implement missions in the vicinity of and on Phobos will require these considerations be taken into account. In this paper the latest published models of the Phobos shape and dynamics are used to characterize its dynamical environment in close proximity orbit about the body, for motion across its surface and for controlled hovering motion in its vicinity. It is found that surface motion is subject to a number of “speed limits” that can cause a moving vehicle to leave the surface and to possibly escape the moon and enter orbit about Mars. In terms of orbital stability, the existence of libration orbit families are characterized down to the surface using an exact potential, and the known stable QSO orbits are shown to be associated with families of stable quasi-periodic orbits.

© 2018 COSPAR. Published by Elsevier Ltd. All rights reserved.

Keywords: Phobos; Small body exploration; Astrodynamics; Surface motion

1. Introduction

The Martian moon Phobos is the current subject of intense scientific speculation regarding its origin and morphological properties such as mass, surface environment and the like. It has been considered to either be a captured asteroid, or the collisional reaggregation of a massive impact crater on the Mars surface (Rosenblatt, 2011). This question is of great interest to planetary science, as either outcome has strong constraints on models of planetary formation and evolution, and would motivate analysis of Phobos samples for different purposes. In addition to the key scientific questions about this body, it also occupies a unique location in the solar system, sitting “on the door-

step” of Mars and providing a simpler and less costly location than the surface of that planet for a variety of exploration motivated applications. Due to these factors, Phobos has consistently been a topic of great interest both for scientific exploration and for human and robotic exploration. There have been several attempts at its exploration, most recently the failed Phobos-GRUNT mission (Marov et al., 2004). Future missions to Phobos are being developed by the Japanese Space Agency with the MMX mission (Kuramaoto, 2016), and continued to be proposed such as the European DePhine mission (Oberst et al., 2017).

The current paper highlights another interesting aspect of Phobos, which is its dynamical environment. This moon is subject to several strong perturbations that make it “extreme” in terms of a highly perturbed environment. These include its strongly non-spherical shape, which has a major influence for motion on and about the body. Due to its orbit about Mars, motion in its environment is also subject to strong tidal forces from Mars (i.e., differential accelera-

* Corresponding author.

E-mail address: scheeres@colorado.edu (D.J. Scheeres).

¹ Currently a post-doctoral scholar at the Jet Propulsion Laboratory, United States.

² Currently a post-doctoral scholar at the Japanese Aerospace Exploration Agency's Institute of Space and Astronautical Sciences, Japan.

tions between rotational effects and gravitational attraction), which in fact makes it unique in the solar system. Related to this, the body also overflows its Roche Lobe, meaning that objects on its surface can have sufficient energy to escape from Phobos and go directly into orbit about Mars. Due to these factors the prospects of motion on the surface of this body are also a subject of interest and studied here. Non-trivial limits to surface motion speeds are found that should be accounted for in any plans for surface mobility. Orbital dynamics about Phobos are also of interest, as any mission to explore this body must first place itself into an appropriate close proximity orbit. Previous orbital studies are extended and show that the previously investigated QSO orbits about Phobos can be computed precisely as quasi-periodic orbits. Finally, given these limitations, the dynamics of controlled hovering motion in the Phobos environment are mapped, as this could also serve as a useful mode of motion in the close proximity environment.

Previous studies of dynamics in the Phobos system have been made, with a few that focus on both orbital and surface motion. [Wiesel \(1993\)](#) presented an analysis of motion in this system using simplified shape model for Phobos. [Dobrovolskis and Burns \(1980\)](#) analyzed motion from the surface and studied its tidal stresses. More recently, [Zamaro and Biggs \(2015\)](#) performed a systematic study of the system using both ellipsoidal and shape-based models. Their focus was mainly on trajectories close to and associated with the libration orbits, for both the case of a circular and elliptic Phobos orbit. Their comprehensive analysis also includes issues related to landing trajectories on this body, generally starting from the vicinity of the libration points. In [Zamaro and Biggs \(2016\)](#) a system analysis of orbit and landing options are made with a focus on how these approaches can be implemented. Our current study is motivated by the lack of a detailed analysis of dynamics on the Phobos surface, or the use of a gravity field not fully consistent with the Phobos shape. It is noted that Zamaro and Biggs in [Zamaro and Biggs \(2015\)](#) used a spherical harmonic expansion to model the surface and near-surface gravity field, which is known to be inaccurate when evaluating the potential and its gradient close to the surface ([Scheeres et al., 2016](#)). Our study also considers surface motion issues, revisits some specific orbit computations and considers orbital stability issues, and maps out the stability regions for hovering motion using previously defined methodologies.

The paper is organized as follows. First, the basic models and equations of motion used in this study are defined. A few different versions of the equations of motion are utilized, and the motivation for these different models are given. Following this, the surface environment and its associated dynamics are explored. This includes deriving specific “speed limits” on motion, beyond which an object would enter a ballistic orbit. The following section reconsiders some aspects of orbital dynamics about the libration points, accounting for a more accurate gravitational field, and discusses the basic properties of stable, retrograde

orbits accounting for the non-circular Phobos orbit. The paper ends with an analysis of the stability and implied navigation implementation needed for maintaining hovering motion at any point about the body.

2. Model for motion in the Phobos system

2.1. Phobos shape and gravity model

Recent observations taken by the Mars Express space-craft enabled the development of a Phobos shape model of significantly higher resolution than has existed. [Willner et al. \(2014\)](#) used this new data to construct a 45 degree and order spherical harmonic model of Phobos, which captures significant surface detail and provides a continuous shape representation. In this model, the radius ρ of a surface point is expressed using Fourier series function of its latitude ϕ and longitude λ , as:

$$\rho(\phi, \lambda) = \sum_{j=0}^J \sum_{k=0}^j [A_{jk} \cdot \cos(k\lambda) + B_{jk} \cdot \sin(k\lambda)] \cdot P_{jk}(\sin \phi) \quad (1)$$

where A_{jk} and B_{jk} are the degree j and order k spherical harmonic coefficients, P_{jk} is the corresponding associated Legendre function, and J is the maximum degree of the considered shape model. The left side of [Fig. 1](#) shows the Phobos shape that is constructed using this model.

Although the shape of Phobos has been measured using imaging techniques, only the central gravity term has been estimated to date, with even the lower order gravity field coefficients being inaccessible without a dedicated close-proximity orbital mission. Thus a constant density gravity field is used for our gravitational model. With this assumption it is possible to define a gravitational field using a series expansion similar to that of Eq. (1) as is done in [Zamaro and Biggs \(2015\)](#). Unfortunately, this series diverges from truth when evaluated close to or inside of the circumscribing sphere of the considered shape. In order to study the surface dynamics of a body, for which gravity field evaluations on the surface are necessary, one therefore cannot use spherical harmonics for gravitational computations and should instead make use of the constant-density polyhedron model ([Werner and Scheeres, 1997](#)). This model can be evaluated both inside and outside of the circumscribing sphere of a body, and is therefore well-suited to perform gravity field evaluations on the surface.

We construct the polyhedron-equivalent of Phobos’ spherical harmonic shape by tessellating the shape model such that the resulting polyhedron has 2562 vertices; this model is shown on the right-hand side of [Fig. 1](#). By combining the computed volume of this polyhedron and the total mass of Phobos $M = 10,678 \times 10^9$ kg ([Pätzold et al., 2014](#)), the corresponding polyhedron density is computed as $\sigma_{poly} = 1.8611 \text{ g/cm}^3$. For comparison, Willner et al. use a bulk density of $\sigma_{sh} = 1.8600 \text{ g/cm}^3$ for Phobos’ spherical harmonic shape with the same mass assumed,

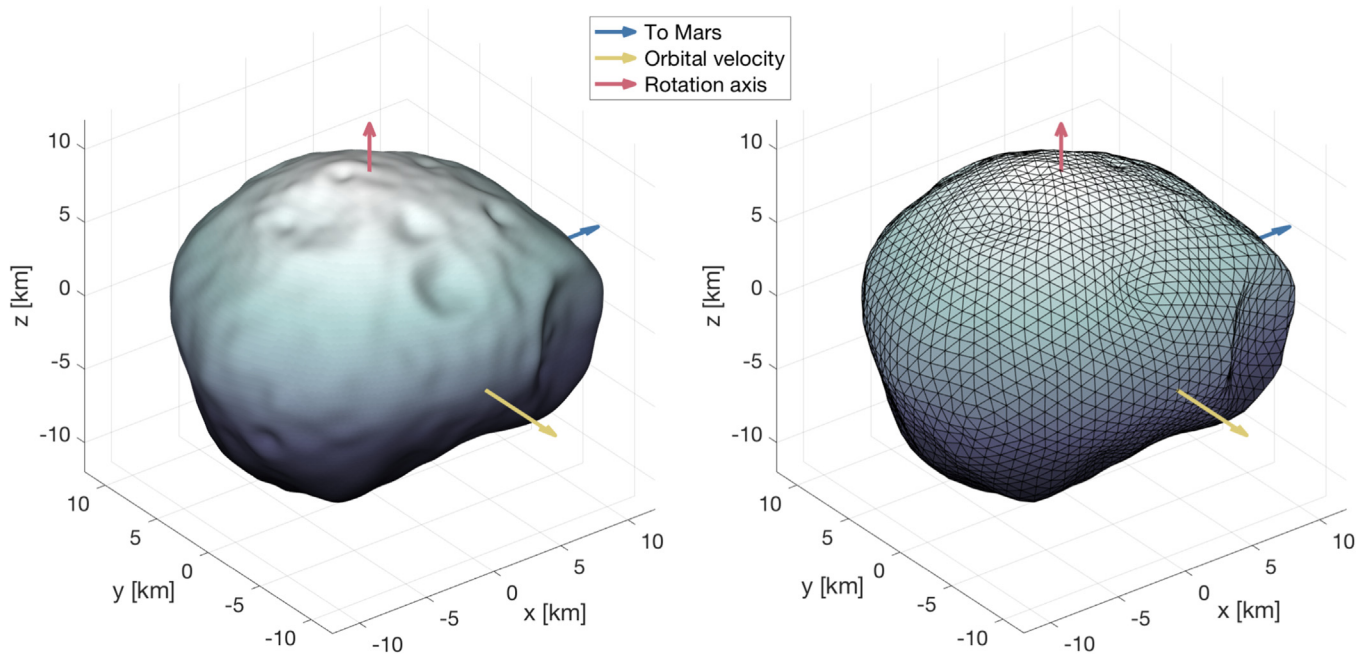


Fig. 1. (left) Degree and order 45 spherical harmonics and (right) polyhedron shape model of Phobos.

implying that the volume between the spherical harmonics and polyhedron are within 0.1%. Given this density value the gravitational potential $U(\mathbf{r})$, acceleration $\nabla U(\mathbf{r})$, and gravity gradient matrix $\nabla \nabla U(\mathbf{r})$ can be specified at any position $\mathbf{r} = [x, y, z]^T$ near or on Phobos, using the formulae summarized in Scheeres (2012). Using the constant density model one can also compute the spherical harmonics coefficients to any order. Table 3 in the Appendix gives the constant density gravity coefficients up to degree and order 4. These coefficients can only be used outside of the circumscribing sphere about Phobos, in general at a radius greater than 13 km. Fig. 2 shows the relative error in the spherical harmonic gravity field acceleration and potential as compared to the exact constant density polyhedron. The large errors, especially in the acceleration, invalidate the use of the spherical harmonic expansion in close proximity to the Phobos surface.

2.2. Spin state

Phobos is trapped in a synchronous rotation state about Mars, with its mean rotation period equal to its Mars orbital period. The key parameters of total gravitational parameter, sidereal spin period and rate, semi-major axis and eccentricity are given in Table 1 (Willner et al., 2010). Due to its eccentric orbit, the difference between its constant rotation angle and the true anomaly equals $-2e \sin M + O(e^2)$, where M is the mean anomaly of its orbit. Given the orbit eccentricity, its geometric libration angle can be estimated from this difference and is 1.7° . On the other-hand, measurements and models predict an additional libration of up to 1.2° , due to the torques from Mars acting on its mass distribution and its free libration (Willner et al., 2010), although other estimates are smaller (Oberst et al., 2014; Burmeister et al.,

2018). While the geometric libration angle is periodic, the free libration angle is not in the rotating frame, due to the mis-match between the oscillation period and the orbit period. The following neglects the free libration, but will include the geometric libration due to the eccentric orbit at some key points of the analysis. Generally, this libration angle is small and its effect can be ignored. However for the stability discussion of orbital dynamics we consider the effect of this libration.

Our general approach to the analysis takes a principal axis coordinate frame fixed in Phobos, with its x -axis pointed towards Mars and its z -axis normal to its orbit plane. Due to our neglect of the free and forced librations, this frame will have a constant rotation rate. However, due to the eccentric orbit there will be a libration between the model x -axis and the Phobos-Mars line connecting the centers of mass. When this effect is taken into account, the Phobos body-fixed frame must be transformed to the Phobos-Mars frame, and vice versa. The matrix $[SB]$ takes the Phobos body frame into this orbital frame and is given by

$$[SB] = \begin{bmatrix} \cos \phi, & \sin \phi, & 0 \\ -\sin \phi, & \cos \phi, & 0 \\ 0, & 0, & 1 \end{bmatrix} \quad (2)$$

where the libration angle $\phi = v - M$ is equal to the instantaneous difference between v and Phobos' mean anomaly M . The transpose of this matrix $[BS] = [SB]^T$ takes the orbit frame into the Phobos body frame.

2.3. Equations of motion

Dynamical computations are carried out with respect to a Phobos-fixed rotating frame. In the following the most

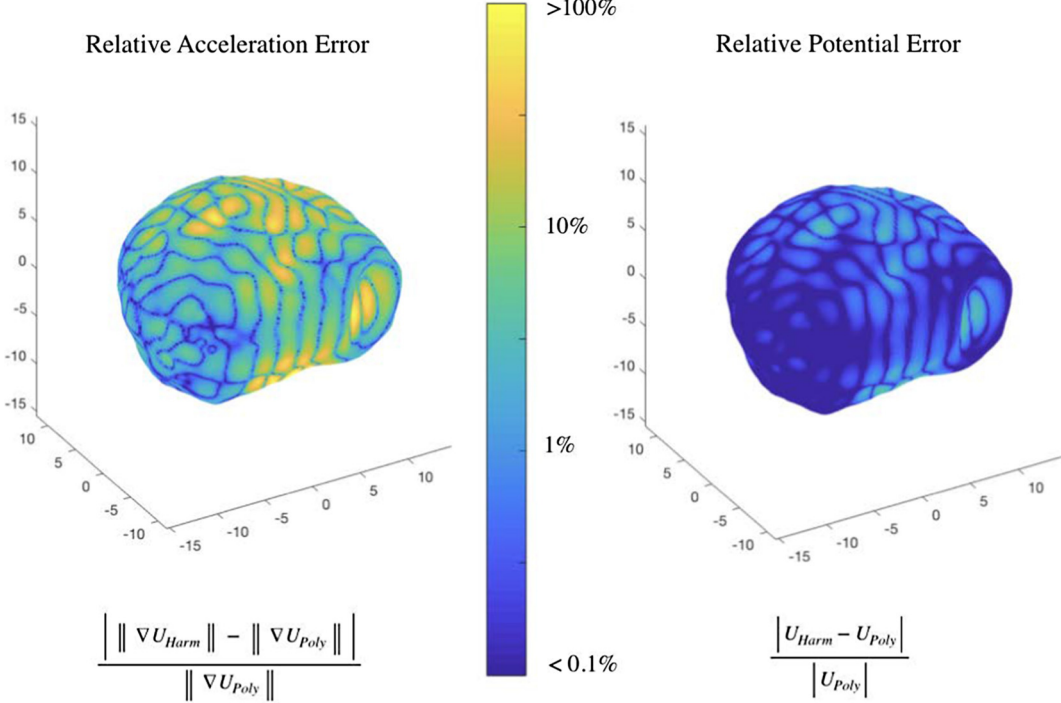


Fig. 2. Relative error mapped on the surface of Phobos, comparing the polyhedral gravitation potential with the gravitational field expanded to 16th degree and order. (Left) shows the relative error in the acceleration, which approaches a factor of 10. (Right) shows the relative error in the potential, which is more subdued yet approaches a factor of unity. The highest errors for both occur at the South pole and are not visible from the given views.

Table 1
Key physical and environmental properties of Phobos.

μ_{Phobos}	$7.13 \times 10^{-4} \text{ km}^3/\text{s}^2$
T_{Phobos}	7.65333 h
ω_{Phobos}	$2.27986 \times 10^{-4} \text{ rad/s}$
a_{Phobos}	9375 km
e_{Phobos}	0.0151

general form of the equations are derived first, as is fitting, and then a few key assumptions are introduced which are used selectively in our later analysis. The net acceleration experienced by a particle with position \mathbf{r} and velocity $\dot{\mathbf{r}}$ in the Phobos-fixed frame can be expressed as (Scheeres, 2012):

$$\ddot{\mathbf{r}} = \nabla U(\mathbf{r}) - \boldsymbol{\omega} \times \boldsymbol{\omega} \times \mathbf{r} - 2\boldsymbol{\omega} \times \dot{\mathbf{r}} + \mu_M \cdot \left(\frac{\mathbf{r}_M - \mathbf{r}}{|\mathbf{r}_M - \mathbf{r}|^3} - \frac{\mathbf{r}_M}{|\mathbf{r}_M|^3} \right) \quad (3)$$

where $\boldsymbol{\omega} = n\hat{\mathbf{z}}$ is the angular velocity of Phobos and $n = \sqrt{\mu_M/a_P^3}$ is the mean motion of Phobos about Mars, where $\mu_M = 4.2828372854 \times 10^4 \text{ km}^3/\text{s}^2$ is the gravitational parameter of Mars and a_P is the semi-major axis of Phobos about Mars given in Table 1. The vector \mathbf{r}_M is the instantaneous position of Mars relative to the Phobos frame as calculated using its 2-body orbital elements, \mathbf{r} is the position of a material point in this frame and the dots signify time derivatives relative to this rotating frame. In general the position of Mars relative to Phobos will oscillate over an

orbit period due to the eccentricity, which is modeled as being due to the difference between the true anomaly and the mean anomaly under the assumption that Phobos uniformly rotates relative to inertial space with its rotation period equal to the Phobos orbital period. Eq. (3) has four acceleration terms: the gravitational attraction from Phobos $\nabla U(\mathbf{r})$, centrifugal acceleration $-\boldsymbol{\omega} \times \boldsymbol{\omega} \times \mathbf{r}$, Coriolis acceleration $-2\boldsymbol{\omega} \times \dot{\mathbf{r}}$, and the tidal acceleration from Mars. The Coriolis acceleration is zero for stationary particles on the surface, of course.

Neglect of the eccentricity will only provide small differences with the exact computations, however the few areas where the eccentricity may become important and must be accounted for are indicated. Unless otherwise specified, it will be assumed that Phobos is in a circular orbit. Under a circular orbit assumption the equations of motion simplify to

$$\ddot{\mathbf{r}} = \nabla U(\mathbf{r}) - \boldsymbol{\omega} \times \boldsymbol{\omega} \times \mathbf{r} - 2\boldsymbol{\omega} \times \dot{\mathbf{r}} + \mu_M \cdot \left(\frac{a_P \hat{\mathbf{x}} - \mathbf{r}}{|\mathbf{a}_P \hat{\mathbf{x}} - \mathbf{r}|^3} - \frac{\hat{\mathbf{x}}}{a_P^2} \right) \quad (4)$$

where $\hat{\mathbf{x}}$ is the unit vector that points towards Mars.

We note that Eq. (3) corresponds to the acceleration of a particle in the elliptic, restricted 3-body problem, though the gravitational field of the secondary body is a general mass distribution and not a point mass and the frame is not the common pulsating frame. Eq. (4) corresponds to the circular-restricted 3-body problem with a general mass distribution for the secondary. It is important to note that

under the circular orbit assumption the equations of motion in the body-fixed frame are time invariant, meaning that a Jacobi integral exists for them.

2.4. Hill approximation

To make some of the analytical computations used later more tractable it is also convenient to introduce the Hill approximation. This assumes that the Mars-Phobos distance is much greater than the particle-Phobos distance, *i.e.*, $a_P \gg r$, and that the mass of Phobos is much smaller than the mass of Mars. Then the circular equations of motion Eq. (4) can be significantly simplified. This results in the famous *Hill 3-body problem*, in which the equations of motion are given as (Scheeres, 2012):

$$\begin{bmatrix} \ddot{x} \\ \ddot{y} \\ \ddot{z} \end{bmatrix} = \omega \begin{bmatrix} 2\dot{y} \\ -2\dot{x} \\ 0 \end{bmatrix} + \omega^2 \begin{bmatrix} 3x \\ 0 \\ -z \end{bmatrix} + \begin{bmatrix} U_x \\ U_y \\ U_z \end{bmatrix} \quad (5)$$

with the usual point mass term replaced by the gradient of the full gravitational force potential of Phobos. The accuracy of this approximation can be questioned, as Phobos' orbit lies a mere 2.4 Mars radii away from the Mars surface. To quantify this accuracy, distributions of the net surface acceleration across Phobos' surface are generated with both the full and simplified equations to find the relative error at each point. These distributions are shown on Mollweide contour plots in Fig. 3. Inspecting this figure, one will find that the two expressions are indeed in very close agreement, with the largest error at the anti-Mars point at 0.08%. This allows the use of the simplified expression to evaluate the net acceleration on a particle in the Phobos environment.

2.5. Normalized and pulsating equations of motion

In anticipation of the orbital analysis the normalized and pulsating equations of motion for the elliptic problems are also derived. For the orbital evaluations the computations are performed in the normalized systems, and the results are rescaled to a dimensional system for reporting the result. For the circular case, a time scale can be defined

which is equal to the inverse of the mean motion of the Phobos orbit, $1/\omega$ and a length scale equal to $(\mu_{Phobos}/\mu_M)^{1/3}a_P$. The normalized gravitational potential is denoted as \bar{U} and lead to the dimensionless equations of motion

$$\begin{bmatrix} \ddot{x} \\ \ddot{y} \\ \ddot{z} \end{bmatrix} = \begin{bmatrix} 2\dot{y} \\ -2\dot{x} \\ 0 \end{bmatrix} + \begin{bmatrix} 3x \\ 0 \\ -z \end{bmatrix} + \begin{bmatrix} \bar{U}_x \\ \bar{U}_y \\ \bar{U}_z \end{bmatrix} \quad (6)$$

where the leading term on the normalized gravitational potential is of the form $\bar{U} = 1/\sqrt{x^2 + y^2 + z^2} + \dots$

For the elliptic case, the resulting equations of motion are simpler if transformed to the Phobos true anomaly as the independent parameter, denoted as v with time derivatives denoted with a $()'$, and scale the length scale by the changing radius (with the same length scale) which results in a variation of the elliptic-Hill 3-body problem (Scheeres, 1998).

$$\begin{bmatrix} X'' \\ Y'' \\ Z'' \end{bmatrix} = \begin{bmatrix} 2Y' \\ -2X' \\ 0 \end{bmatrix} + \frac{1}{1+e\cos v} \left\{ \begin{bmatrix} 3X \\ 0 \\ -Z \end{bmatrix} + [SB] \begin{bmatrix} \bar{U}_x \\ \bar{U}_y \\ \bar{U}_z \end{bmatrix} \right\} \quad (7)$$

This equation is oriented along the instantaneous Phobos-Mars line, and thus the Phobos gravity field will librate relative to this frame (designated with capital letters).

3. Surface dynamical environment

Using the previously defined models and accelerations the environment on the surface of Phobos is analyzed. Following this a characterization of kinematic limits on the speed and direction of surface motion to ensure that a vehicle would stay on the surface, and global speed limits to ensure that it remains trapped to Phobos. We note that the study in Zamaro and Biggs (2015) considered some aspects of the gravitational potential in the proximity of and on the surface of Phobos. However, as they used a spherical harmonic potential, the errors in those computa-

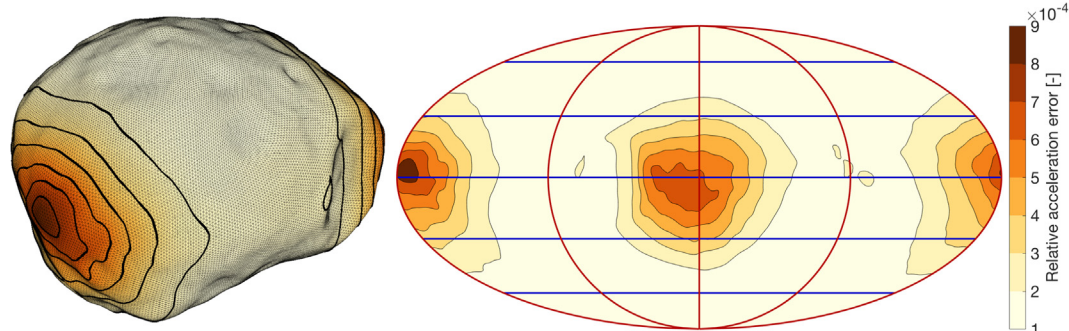


Fig. 3. Relative acceleration error between the Hill approximation and the full tidal force. These results are both overlaid on Phobos's three-dimensional shape model and with a two-dimensional Mollweide plot (defined in Appendix).

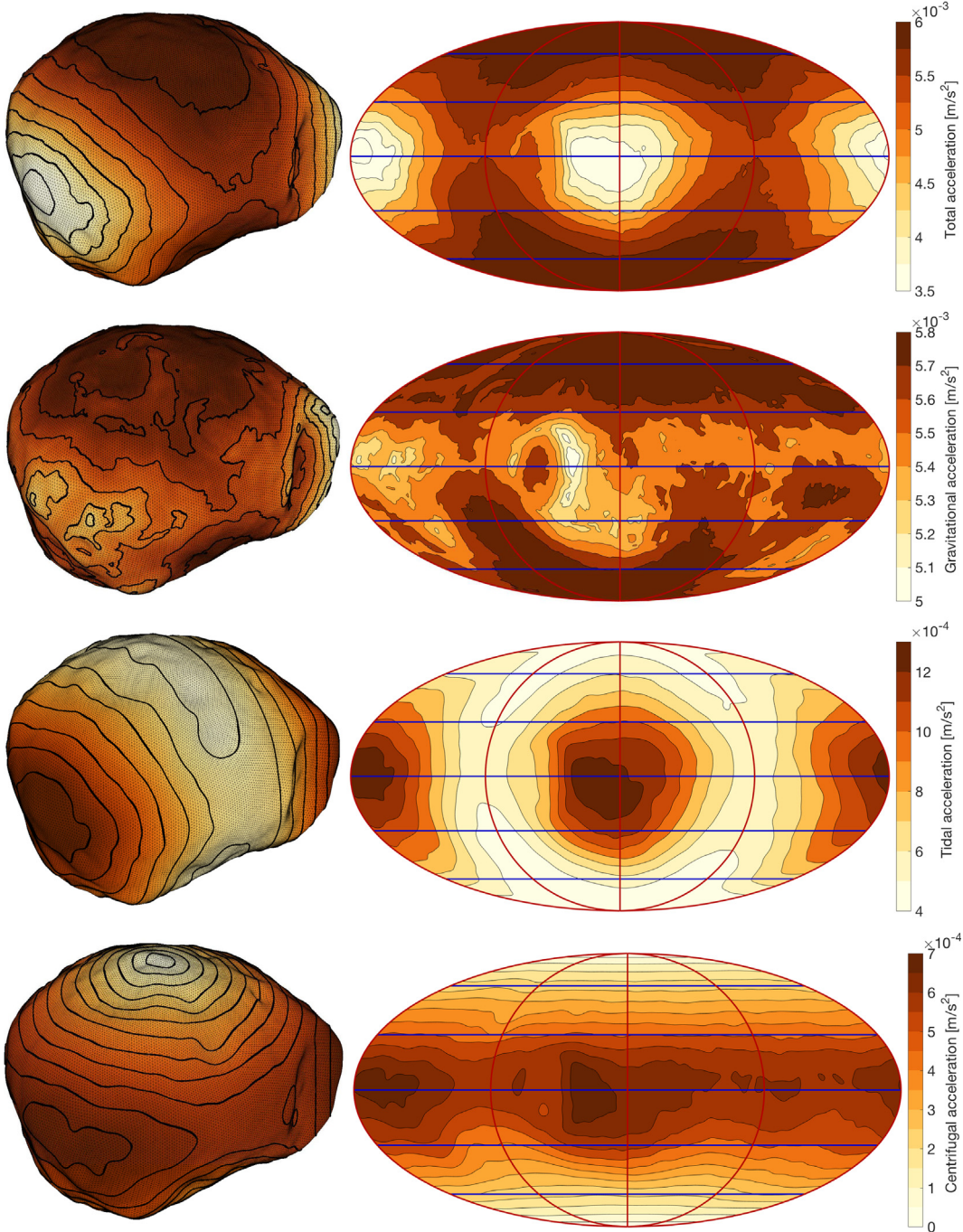


Fig. 4. From top to bottom: the net, gravitational, tidal, and centrifugal acceleration distributions across the surface of Phobos.

tions are significant enough so that we revisit all relevant surface computations here.

3.1. Acceleration components

Eq. (3) provides the different acceleration components present on the surface of Phobos. Fig. 4 shows the distribution of the net acceleration magnitude across the Phobos surface, as well as the three relevant components (the Coriolis acceleration is not shown as it has zero magnitude for stationary surface particles). Each acceleration is shown on

both a Mollweide projection latitude-longitude map (defined in Appendix) and on the three-dimensional Phobos shape; the color scale and contour lines of both plots are equivalent. These results show that the gravitational acceleration dominates the Phobos surface environment, with smaller contributions by the tidal and centrifugal accelerations. Table 2 provides approximate magnitudes of the separate acceleration components corresponding to Phobos gravity, Mars' gravity, and centrifugal at, respectively, the poles, leading/trailing edges, and sub-/anti-Mars points. As the accelerations act in different directions,

Table 2
Acceleration magnitudes in mm/s².

Acceleration	Poles	Leading/trailing	Sub/anti-Mars
Total	6.3	5.6	3.5
Gravitational	5.8	5.6	5.4
Tidal	0.4	0.6	1.3
Centrifugal	0.0	0.6	0.6

their magnitudes do not necessarily add up to the magnitude of the total acceleration.

3.2. Surface slope

Using the net acceleration provided by Eq. (5) the local slope θ can be computed across the surface of Phobos as:

$$\theta = \arccos \left(\frac{\hat{\mathbf{N}} \cdot \ddot{\mathbf{r}}}{\|\ddot{\mathbf{r}}\|} \right) \quad (8)$$

in which $\hat{\mathbf{N}}$ is the surface normal computed from the spherical harmonic expression as:

$$\hat{\mathbf{N}} = \frac{\mathbf{u}_\phi \times \mathbf{u}_\lambda}{\|\mathbf{u}_\phi \times \mathbf{u}_\lambda\|} = \frac{\mathbf{u}_\phi \times \mathbf{u}_\lambda}{\sqrt{\mathbf{u}_\phi \cdot \mathbf{u}_\phi + \mathbf{u}_\lambda \cdot \mathbf{u}_\lambda + (\mathbf{u}_\phi \cdot \mathbf{u}_\lambda)^2}} \quad (9)$$

where $\mathbf{u} = \rho(\phi, \lambda) \cdot [\cos \phi \cos \lambda, \cos \phi \sin \lambda, \sin \phi]^T$, where ϕ and λ are the latitude and longitude again and the subscripts denote partial differentiation. For an expression of the partial derivatives in this expression, the reader is referred to Van wal and Scheeres (2017). The resulting slope distribution is included in Fig. 5 and shows slopes of up to 45°, though most surface regions have a slope smaller than 15°. As expected, the highest slopes are found on crater rims, particular in the Stickney crater. These results match those computed by Willner et al. (2014), providing a check on our implementation. The histogram and corresponding cumulative distribution function of the surface slopes are shown in Fig. 6.

3.3. Energy and velocities

Although the motion of a particle in the Phobos neighborhood does not have any analytical solutions, the 3-body

motion expressed by Eqs. (4) and (5) does permit one integral of motion that provides insight into the feasible trajectories of a particle (note, the full system incorporating the orbital eccentricity does not admit an integral). This integral is commonly known as *Jacobi's integral* for the restricted 3-body problem. Using our Phobos-fixed frame and the equations given in Eq. (5), the integral is stated as:

$$C = \frac{1}{2} v^2 - \left[\frac{1}{2} \omega^2 (3x^2 - z^2) + U(\mathbf{r}) \right] \quad (10)$$

and represents the total energy of a particle in the Phobos-fixed frame. This invariant may be used to study regions within the 3-body system that are accessible to the particle, given some set of initial conditions. By setting $v = 0$ and evaluating Eq. (10) across Phobos' surface, the energy of stationary particles on the surface can be determined (Fig. 7).

It is interesting to note that the maximum regions of potential energy on the Phobos surface are located at the leading and trailing edges of this body. Note that for a simple sphere, one would expect the highest potential energy to be at the polar regions, and equal to $[\frac{1}{2} \omega^2 R^2 - \mu/R]$. This implies that the shape of Phobos has altered the potential energy of the surface, and may indicate an additional physical evolution phenomenon that would result in this deviation.

These energy values can be used to find the amount of kinetic energy which can be gained when moving over the surface (from a high potential area to a low potential area), or signify the level of kinetic energy which must be added to orbitally access higher regions in the gravitational potential. Across the Phobos surface the maximum potential energy occurs at the leading and trailing edges and is approximately $C_{max} = -60.40$ (m/s)², while the lowest potential lies within the Stickney crater and equals $C_{min} = -74.21$ (m/s)². If a particle were to travel, without energy loss, from the highest to the lowest region it would then gain $\frac{1}{2} V^2 = C_{max} - C_{min}$ kinetic energy, or a speed of $V = \sqrt{2(C_{max} - C_{min})} \sim 5.3$ m/s. Conversely, a particle given this speed in Stickney crater (or at any point of the body) would in principal have sufficient energy to traverse to the highest energy point on Phobos.

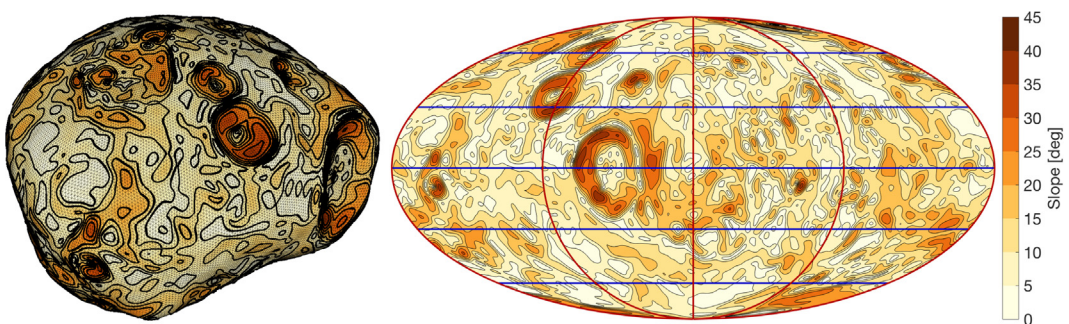


Fig. 5. Slope distribution across the surface of Phobos.

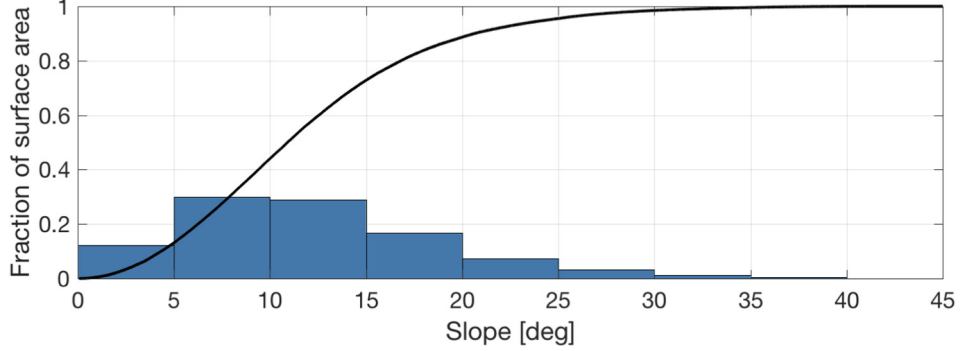


Fig. 6. Slope distribution statistics of Phobos.

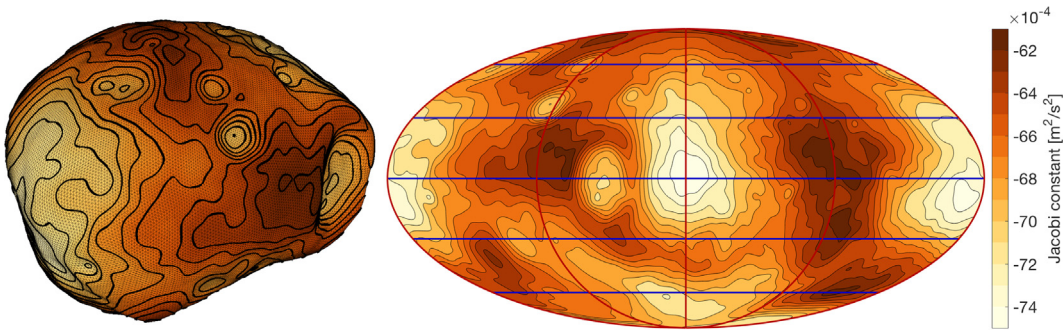


Fig. 7. Jacobi constant distribution across the surface of Phobos.

3.4. Equilibrium points and Roche lobe

The distribution of the Jacobi constant C is also plotted across the xy -plane of the system as shown in Fig. 8. Note the two singular points, which correspond to the well-known equilibrium points in the Hill problem. For the ideal Hill problem the location of these equilibria would be at $x = \pm (\frac{\mu_M}{3\omega^2})^{1/3} a_p$, however at Phobos their location is

shifted due to the non-spherical gravitational field. To compute them precisely equation $\nabla C = \mathbf{0}$ is iteratively solved using a Newton-Raphson method to find the positions of the L_1 and L_2 equilibrium points.

$$\mathbf{r}_{L_1} = \begin{bmatrix} 17.366 \\ -0.435 \\ -0.322 \end{bmatrix} \text{ km} \quad \text{and} \quad \mathbf{r}_{L_2} = \begin{bmatrix} -17.246 \\ -0.514 \\ -0.096 \end{bmatrix} \text{ km} \quad (11)$$

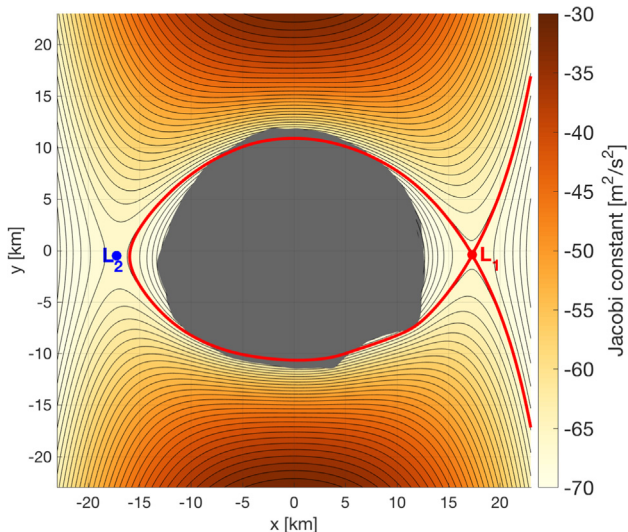


Fig. 8. Zero-velocity curves, equilibrium points and Roche lobe of Phobos.

which have corresponding Jacobi constants $C_{L_1} = -66.34$ and $C_{L_2} = -65.88$. **Jacobi in m^2/s^2 !**

Included in Fig. 8 are also the equipotential lines within the xy -plane that have the same Jacobi constant (and therefore the same energy level) as the L_1 point. For the L_1 point, the resulting closed curve is known as the *Roche lobe* (Dobrovolskis and Burns, 1980). All stationary particles that lie within this lobe are energetically bound to remain in Phobos' vicinity; particles outside of the lobe are not. This means that, energetically, any stationary particle located outside of the Roche lobe could escape Phobos' vicinity through the neck region around L_1 and depart on some orbit that takes it further away from Phobos (return to Phobos is possible, but not guaranteed within finite time). Inspecting Fig. 8, one finds that Phobos' leading and trailing edges partially lie outside of this Roche lobe. Particles on these edges are therefore not energetically bound to Phobos, and could escape through the L_1 neck region, if they can find a trajectory that does not intersect

the surface. A similar curve can be constructed using the energy level of the L_2 point; as the two equilibrium points have highly similar energy levels, the L_1 lobe lies very close to the L_2 Roche lobe. Most particles on the leading/trailing edge therefore also have the energy to escape through L_1 or L_2 . However, this does not mean those particles have a physical path along which to escape. Indeed, a stationary particle on Phobos' leading/trailing edge would have to burrow through the surface in order to reach either of the neck regions.

This is illustrated on the left-hand side of Fig. 9, where a particle is released with zero velocity on the leading edge of Phobos and allowed to pass through the satellite's surface unobstructed, while following the gradient of the polyhedron potential which is well defined in the interior. After a short chaotic orbit that mostly lies inside of Phobos' surface for approximately 10 h, the particle escapes through the L_2 neck region. The dark regions in this figure are the inaccessible regions corresponding to the particle's Jacobi constant.

3.5. Guaranteed return speed

Stationary particles outside of the L_1 and L_2 Roche lobes have sufficient energy to escape their respective neck regions; particles within these lobes do not, and are therefore bound to remain within Phobos' vicinity. However, when the latter are given some speed v , their energy as given by the Jacobi constant C increases, such that the neck regions may open up and allow departure from Phobos. The necessary speeds for this to occur can be computed from Eq. (10) as:

$$V_i = \begin{cases} \sqrt{2(C - C_{L_i})} & \text{if } C - C_{L_i} > 0 \\ 0 & \text{if } C - C_{L_i} \leq 0 \end{cases} \quad (12)$$

where C is the Jacobi constant of the considered surface location. The speed V_i is the *guaranteed return speed* (Scheeres et al., 1996), as particles with a speed lower than V_i cannot pass through the corresponding neck region and escape the Phobos vicinity. Particles with a lower speed are therefore guaranteed to remain inside the Roche Lobe and eventually return to the surface. The surface distributions of V_1 and V_2 are shown in Fig. 10. Following the difference in L_1 and L_2 energy levels, the escape speeds V_2 are slightly higher than the guaranteed return speeds V_1 . In addition to the leading and trailing edges, particles on Phobos' northern pole also have sufficient energy to escape. This suggests that surface mobility operations are safest when carried out at the sub- and anti-Mars points, and at the southern pole as vehicles operating on these regions do not have sufficient energy to escape Phobos' vicinity. Craft operating on the leading/trailing edges or on the northern pole could escape through either L_1 or L_2 after a small hop, either intentionally or unintentionally. This is illustrated on the right-hand side of Fig. 9, where a particle departs from the rim of Stickney crater with a velocity $v = [4.0, 1.5, 0]^T$ m/s. After grazing the opposite crater rim, the particle escapes the Phobos vicinity through the L_1 neck region. An alternate pathway to escape could also be a particle sliding or rolling down from a potential high and achieving ballistic flight with sufficient energy to escape. This scenario is investigated in the next subsection. Again, the dark regions are the inaccessible regions corresponding to the particle's Jacobi constant.

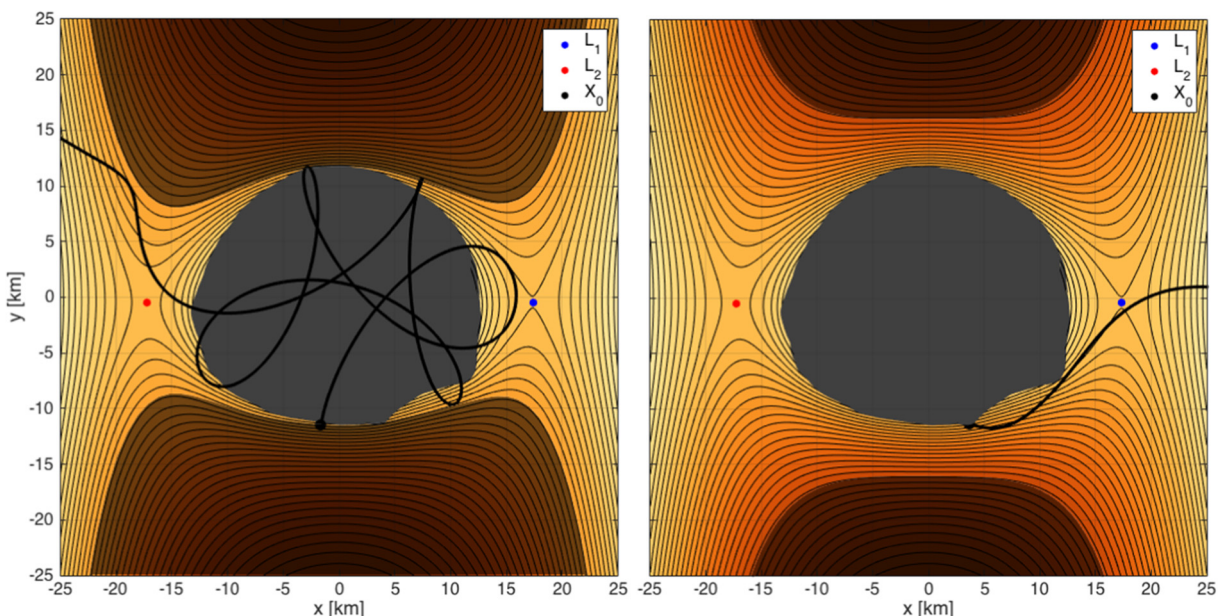


Fig. 9. Sample trajectories of a particle departing with (left) zero velocity and (right) $v = 4.3$ m/s from the surface of Phobos.

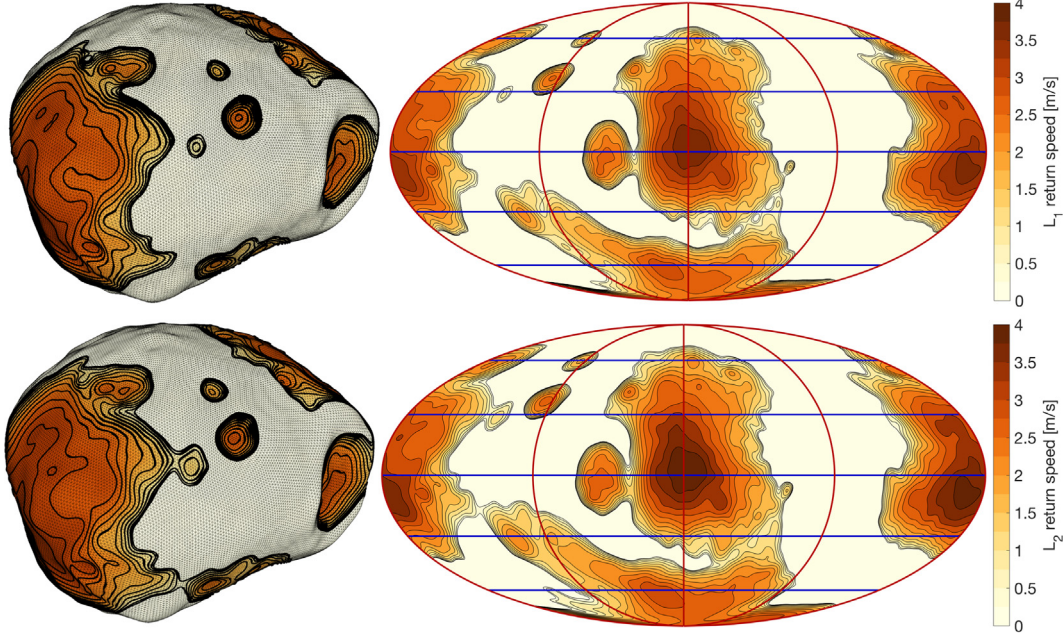


Fig. 10. Guaranteed return speeds for the L_1 (top) and the L_2 (bottom) neck regions.

Note that the regions of positive return speed are separated from each other, thus technically only those regions that have a direct connection with the corresponding libration point can lead to escape at speeds greater than this amount. This is a unique situation for Phobos where these regions are separated (or narrowly connected at best) between L_1 and L_2 . Furthermore, large regions on the leading and trailing edge of the body and its north pole are above the energy of the libration points. This situation is due to Phobos overflowing its Roche Lobe, as initially discovered by Dobrovolskis and Burns (1980). This may either be due to the body's slow migration to lower radii, or could be due to ejecta from previous impacts blanketing the Phobos surface and building up its size. The fact that these regions are above the equilibrium point values means that material can drift in “from infinity” and settle in these regions. This latter mechanism could also explain why the leading and trailing edges of Phobos are the potential highs in the system, but is a topic for future study. Finally, one should note that this condition only tracks a particle’s energy, and does not relate to the accelerations acting on it. Thus, even though a particle may be outside the Roche Lobe and susceptible to escape, it will still generally feel a total acceleration that holds it to the surface.

3.6. Lift-off velocity

The return speed provided above is defined energetically and does not restrict the direction of particle motion; both normal and tangential velocity components are allowed. When the particle velocity is restricted to be purely tangential, a different type of ‘speed limit’ can be derived that relates to temporary and local lift-off from the surface. This

lift-off velocity is defined by Van wal and Scheeres (2016) as “*the (tangential) surface velocity given to a particle on a body with arbitrary shape, rotation, and gravity, at which the particle will locally lift off from that surface in its direction of travel.*” It can be expressed as:

$$\mathbf{v}_\theta = v_\theta \hat{\mathbf{b}}_\theta \quad (13)$$

$$v_\theta = \pm \sqrt{\rho_\theta^2 (\hat{\mathbf{b}}_\delta \cdot \boldsymbol{\omega})^2 + \rho_\theta \hat{\mathbf{b}}_\rho \cdot (\tilde{\boldsymbol{\omega}} \cdot \tilde{\boldsymbol{\omega}} \cdot \mathbf{r} - \mathbf{a}_E) - \rho_\theta \hat{\mathbf{b}}_\delta \cdot \boldsymbol{\omega}} \quad (14)$$

in which ρ_θ is the surface radius of curvature in the direction of travel $\hat{\mathbf{b}}_\theta$, which governs the magnitude of the lift-off velocity v_θ . The unit vector $\hat{\mathbf{b}}_\delta$ defines, along with $\hat{\mathbf{b}}_\theta$, the osculating departure plane in which the particle moves. The velocity magnitude varies as a function of the direction of travel, and displays a minimum and maximum that are roughly aligned along and against the local surface rotational velocity. In Phobos’s environment, the external acceleration \mathbf{a}_E is equal to the sum of the gravitational and tidal accelerations from Eq. (3). The centrifugal acceleration is included in the lift-off velocity equation through the $\tilde{\boldsymbol{\omega}} \cdot \tilde{\boldsymbol{\omega}} \cdot \mathbf{r}$ term. For a detailed discussion of the properties of this expression, and computation strategy for ρ for spherical harmonic shapes, the reader is referred to Van wal and Scheeres (2017, 2016).

Fig. 11 shows the surface distribution of minimum and maximum lift-off velocities. It is important to note that lift-off is only possible when the surface is locally convex; black regions in the figures are locally concave (either in some or in all directions) and are therefore given an infinite lift-off velocity. The global minimum lift-off velocity is found to be $v_{\theta,\min} = 1.60$ m/s. Thus, any surface vehicle

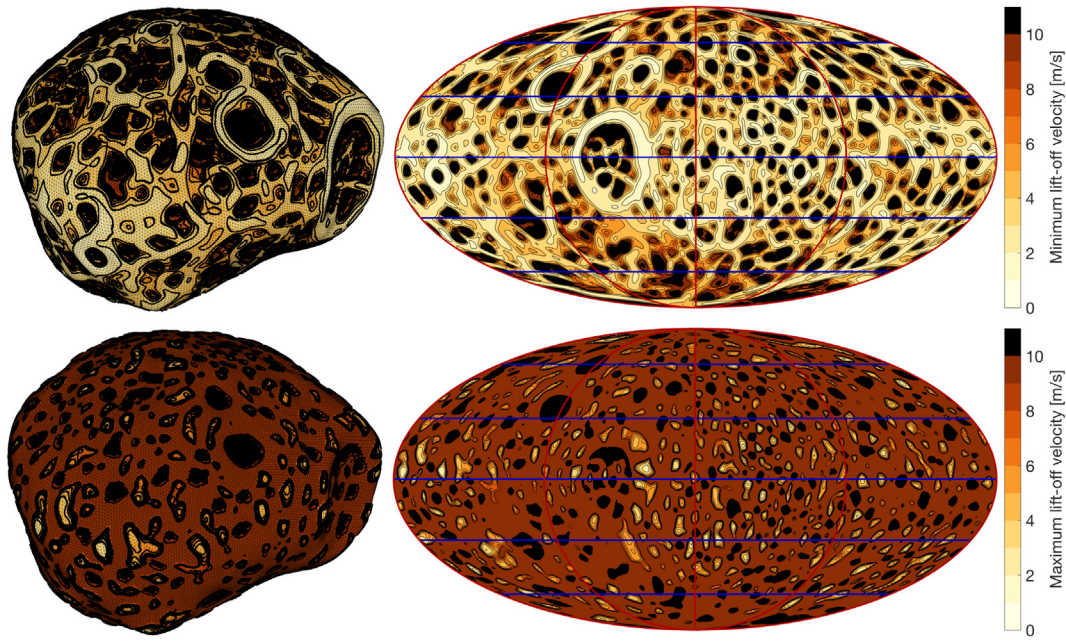


Fig. 11. (top) Minimum and (bottom) maximum lift-off velocity across the surface of Phobos.

operating on the surface of Phobos can safely reach a surface velocity of 1.60 m/s without entering onto a ballistic orbit. Most of Phobos's surface has a minimum lift-off velocity of at least 2 m/s. These minimum velocities generally occur for motion towards the east, along the rotational velocity of Phobos's surface. When an object moves towards the west, against the surface rotation, the lift-off velocity is much higher. In fact, most of Phobos's surface has a maximum velocity of at least 10 m/s, well in excess of the L_1 return velocity. This suggests that vehicles can operate at relatively high velocities in directions opposite Phobos's rotation, however if they do achieve ballistic motion they will be susceptible to escaping from Phobos given their high kinetic energy.

Once lift-off speed is attained the object will be naturally translated into a ballistic orbit whose terminus is not known apriori. While it is possible for the object to reintersect the surface after a brief ballistic period, it is also possible for the object to depart the vicinity where lift-off occurred and be transported to another region of Phobos or even to escape. As the speeds are high enough to be above the guaranteed-return speed over most of the body this remains a possibility. Due to this it will naturally be prudent for vehicles in this environment to stay below these speeds or carry sufficient control authority to thrust back down to the surface if ballistic lift-off is achieved.

In addition to this lift-off velocity across the curved Phobos surface, there exists another lift-off criterion using the local surface normal and net acceleration. This criterion, defined as the *ridge* lift-off speed in Van wal and Scheeres (2016), expresses the speed required for a very brief “air time” after an object with finite radius R rolls off a small ridge or asperity on the surface, such as a rock. This is sim-

ilar to an automobile traversing a bump and becoming temporarily air-borne. This speed is independent of the direction of travel, but does depend on the object radius R , and is equal to:

$$V_R = \sqrt{-R\hat{\mathbf{N}} \cdot \ddot{\mathbf{r}}} \quad (15)$$

where R is the radius of the wheeled vehicle, $\hat{\mathbf{N}}$ is the surface normal and $\ddot{\mathbf{r}}$ is the local total acceleration acting on the vehicle from Eq. (3). Fig. 12 plots the distribution of the *normalized* ridge lift-off velocity, *i.e.*, of V_R/\sqrt{R} . The values shown therefore also correspond to the ridge lift-off velocity of an object with radius $R = 1$ m. These results show that although an object can move on Phobos' surface at velocities of several meters per second without lifting off and entering a global ballistic trajectory, one should expect a reduction in friction/traction with the surface at velocities exceeding roughly 7 cm/s for a 1 m radius wheel due to brief ballistic intervals due to “bumps” on the surface. This particular speed limit reduces with radius, so that at a 0.1 m radius the speed would be on the order of 2.2 cm/s. Note that these limits do not account for the likely granular nature of the Phobos surface, which would require additional analysis techniques.

4. Orbital environment

The Phobos orbital environment is now characterized using previously developed methodologies focusing on planar periodic orbits and quasi-periodic orbits and their stability. A full exploration of the orbital environment about Phobos must also explore out of plane motions, however that would require significant additional material that will

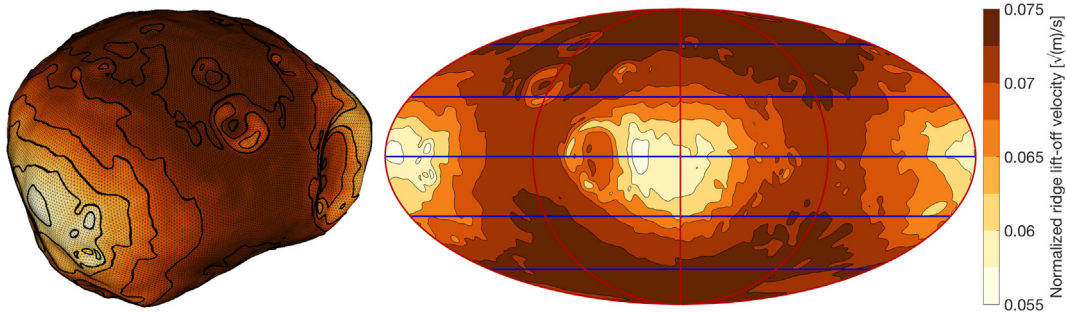


Fig. 12. Normalized ridge lift-off velocity across the surface of Phobos.

be best handled in a follow-on analysis. We consider families that both ignore the eccentricity of Phobos' orbit, and those that account for it. To summarize our conclusions, we find that periodic orbit families about the two libration points are highly unstable and thus should exert a significant influence on close proximity dynamics and will require active controls to maintain. Conversely, retrograde periodic orbits are stable down to the Phobos surface, and their stability persists when accounting for the Phobos eccentricity. The orbital structure about the libration points was studied in great detail in [Zamaro and Biggs \(2015\)](#), and the reader is referred to that paper for a more complete discussion of motion about the libration points. A short section is given herein where an analysis of the families associated with these points is presented, where the families are continued to intersection with the Phobos surface. Given the use of the polyhedron potential herein, these computations are provided for comparison with ([Zamaro and Biggs, 2015](#)), as using their spherical harmonic potential the acceleration errors in close proximity to Phobos would have been subjected to significant errors. It is important to note that our results seem quite consistent with theirs where applicable. One should also note that our approach to the computation of the families in the full system is different than the approach used by [Zamaro and Biggs \(2015\)](#).

4.1. Periodic orbit families about the libration points

Computing periodic orbits about an asymmetric body such as Phobos using a general-purpose periodic orbit computation scheme is not notably more difficult in a model with an irregular gravity field as it is in a “simple” model like the circular restricted 3-body problem (CR3BP). The only real difference is the effort required to implement the equations of motion, but once this is done, it is just an input to the orbit solver. Mapping out the periodic orbit families, however, can be more difficult due to changes in the bifurcation structure which remove the symmetries that exist in ideal problems.

Ignoring the Phobos eccentricity, its shape is fixed in the Hill rotating reference frame allowing us to study the periodic orbits emanating from its libration points. The lack of symmetry of the HR3BP + shape model makes

the periodic orbit computation more challenging since the periodic orbit families no longer intersect with each other (except at the equilibrium points where each Floquet multiplier pair corresponds to an emanating family of periodic orbits). Since bifurcations can be quite helpful for exploring periodic orbit families, we start from an intermediate, symmetric model: HR3BP + ellipsoid. That is, instead of using an irregular shape, Phobos is represented as a uniform density tri-axial ellipsoid whose mass and moments of inertia are the same as the polyhedron's. In all three models (HR3BP, HR3BP + ellipsoid, HR3BP + shape), there are two libration points L1 and L2, though their locations differ between the models. The L1 point lies between Mars and Phobos, and the L2 point is on the far side of Phobos. In all the cases, both libration points have stability (Floquet multiplier pairs) of type: center, center, saddle. As in the usual HR3BP, the two center components in the HR3BP + ellipsoid correspond to planar and vertical periodic orbit families. These are shown in Fig. 13 at top. A notable difference between the HR3BP and the HR3BP + ellipsoid model is that in the latter model the halo orbits (shown in the bottom of Fig. 13) bifurcate from the vertical Lyapunov orbits rather than the planar ones. The bifurcating vertical orbit is shown in red and appears as a thin vertical line.

We can, however, take advantage of the fact that our non-symmetric model is close to a symmetric model. In this case, one can trace out the periodic orbit bifurcation behavior in the symmetric model, then use a homotopy method to move some of these orbits to the non-symmetric model. If the orbit's period is fixed (just one choice), one can use a homotopy parameter $\rho \in [0, 1]$ to move it from the symmetric equations of motion to the non-symmetric ones

$$f(x; \rho) = (1 - \rho)f_{\text{sym}}(x) + \rho f_{\text{non}}(x) \quad (16)$$

In this way one can obtain orbits in the non-symmetric model that are not directly connected to the equilibrium point. Once one orbit on the disconnected branch is found, one can perform continuation of its family strictly in the non-symmetric model. If the non-symmetric model is far from the symmetric model, completely new branches may also appear that are unrelated to any in the symmetric model. These orbits may be more challenging to find, but

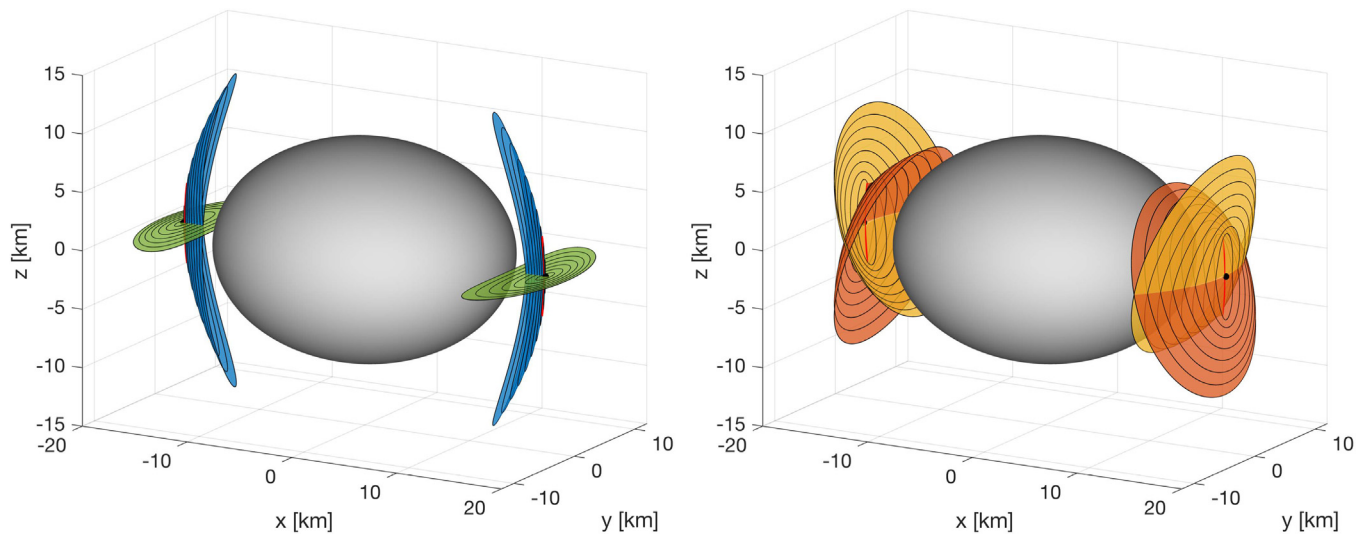


Fig. 13. Periodic orbits for Mars-Phobos HR3BP + ellipsoid model.

it might not always be necessary to find them unless there is a specific need. Due to this property one cannot guarantee that all relevant periodic orbit families have been found.

Periodic orbits computed with this methodology and related to the libration points in the HR3BP + shape model are shown in Fig. 14. Here the planar orbits shown in green have a similar structure to the ellipsoid case, except now these orbits have some small out-of-plane component. However, since the shape model is not symmetric, the bifurcation along the vertical orbit family is no longer present. Instead the small vertical orbits merge into southern halo orbits for L1 (red branch), and the small vertical orbits merge into the northern halo orbits for L2 (yellow branch). For L1, the large vertical orbits (blue) merge into the northern halo orbits (yellow); for L2, the large vertical orbits (blue) merge into the southern halo orbits (red). The approximate turning points are shown as black orbits. Neither of these branches are directly connected to its corresponding libration point. Rather, they were computed by using the homotopy method to move a large vertical orbit from the (symmetric) HR3BP + ellipsoid model to the (non-symmetric) HR3BP + shape model. Then, standard pseudo-arclength continuation could be used to generate the entire branch (including going beyond the turning point).

While the rich structure in these periodic orbit families is of interest, it should be noted that they are all unstable orbits in general. Most relevant, the small interval of stable halo orbits that exist in the Hill problem (Howell, 1984) are not present about Phobos. Thus, while these orbit families control the dynamics about these regions of space, they do not have any direct practical use for long-term orbits in this system as their instability times are quite short. The instability of these orbits, their use as staging orbits for landing on Phobos, and their bifurcation into quasi-periodic orbits is explored in more detail in Zamora and Biggs (2015). The family structure seen here, using the more accurate

polyhedron potential, appears quite similar to that paper, and thus no additional analysis of these is given.

4.2. Stable periodic orbits about Phobos

Next considered are the family of retrograde periodic orbits about Phobos analogous to the stable retrograde orbits in the Hill 3-body problem (Hénon, 1969). When far from the body, these degenerate into the 2:1 ellipse orbits found in the Clohessy-Wilshire equations. In this case, both the stable family when the eccentricity is zero and the quasi-periodic orbits that emerge when non-zero eccentricity are computed. The equations used for these computations were given earlier in Eqs. (6) and (7). Our contribution in this section is to show that the quasi-periodic orbits that emerge from the retrograde periodic orbits remain stable, and thus motion about these orbits will be oscillatory. This establishes a clear connection between these orbits and the quasi-satellite orbits used frequently in mission design studies for Phobos orbiters (Marov et al., 2004).

The discussion is simpler if the problem is restated in state space as

$$\dot{\mathbf{x}} = \mathbf{f}(v, \mathbf{x}) \quad (17)$$

where $\mathbf{f}(v + 2\pi, \mathbf{x}) = \mathbf{f}(v, \mathbf{x})$, $\mathbf{x} = [x, y, z, u, v, w]^T$ represents the state of the vehicle in a pulsating reference frame centered on Phobos and such that $\hat{\mathbf{x}}$ is constantly aligned with the two barycenters of the primaries, $\hat{\mathbf{z}}$ is parallel to the orbital angular momentum of Phobos, and $\hat{\mathbf{y}} = \hat{\mathbf{z}} \times \hat{\mathbf{x}}$ completes the right-handed triad. Finally, v is the true anomaly of the planetary satellite as well as the independent variable of Eq. (7).

4.2.1. Periodic orbits

By inspection of Eq. (7), it is apparent that the equations of motion depend explicitly on the independent variable v .

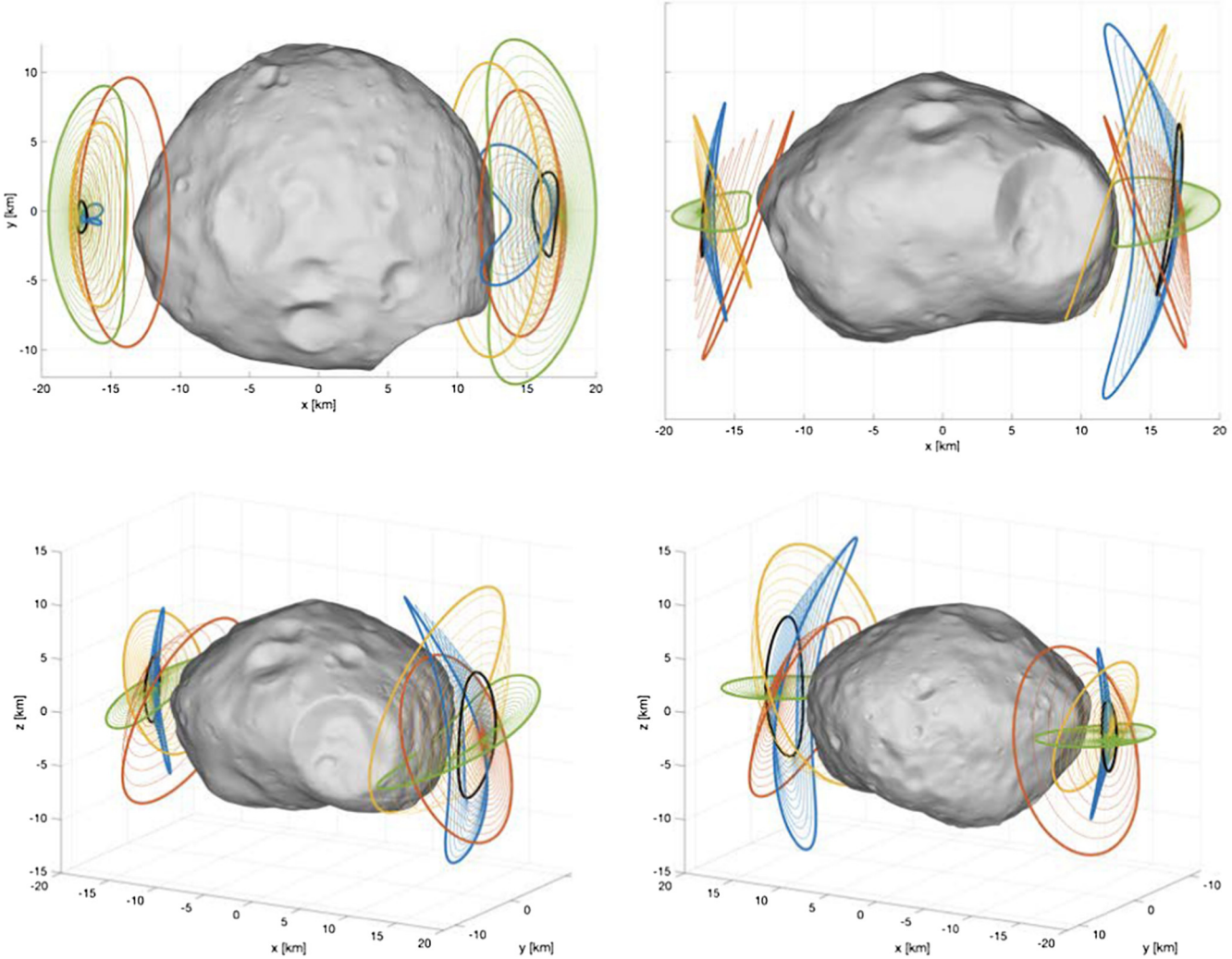
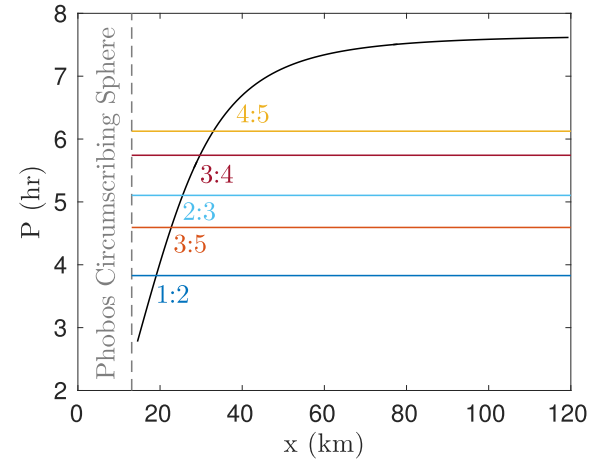


Fig. 14. Periodic orbits for Mars-Phobos HR3BP + shape model.

Consequently, the Elliptical Hill Problem (EHP) is a nonautonomous system that does not depend on any external parameter as long as the eccentricity of the planetary satellite is fixed. Following Broucke (1969), this means that periodic orbits are no longer organized in families but are isolated at best. In particular, the period must be resonant with the periodicity of the equations of motion (7), i.e., with the orbital period of Phobos around Mars.

As an example, consider the family of periodic orbits found in the circular case $e = 0$ when $[SB]$ is also equal to the identity matrix. Fig. 15 displays the chart of the periodic orbit period versus the x -axis crossing with $v < 0$, illustrating that only those whose period is resonant with 2π actually survive when the eccentricity of Phobos is taken into account. Fig. 16 show these orbits on the left. This family of periodic orbits are all stable in the sense that their eigenvalues all lie on the unit circle, thus orbits displaced from these will naturally oscillate about the nominal periodic orbit. This motion has been identified in past studies and these displaced orbits called quasi-satellite orbits (or QSOs). Their properties are very analogous to those about

Fig. 15. Period vs positive x -crossing for the family of quasi-satellite orbits with $e = 0$. Only the periodic orbits whose period is resonant with 2π survive when $e \neq 0$.

the satellite Deimos which was studied in detail in Scheeres (2012).

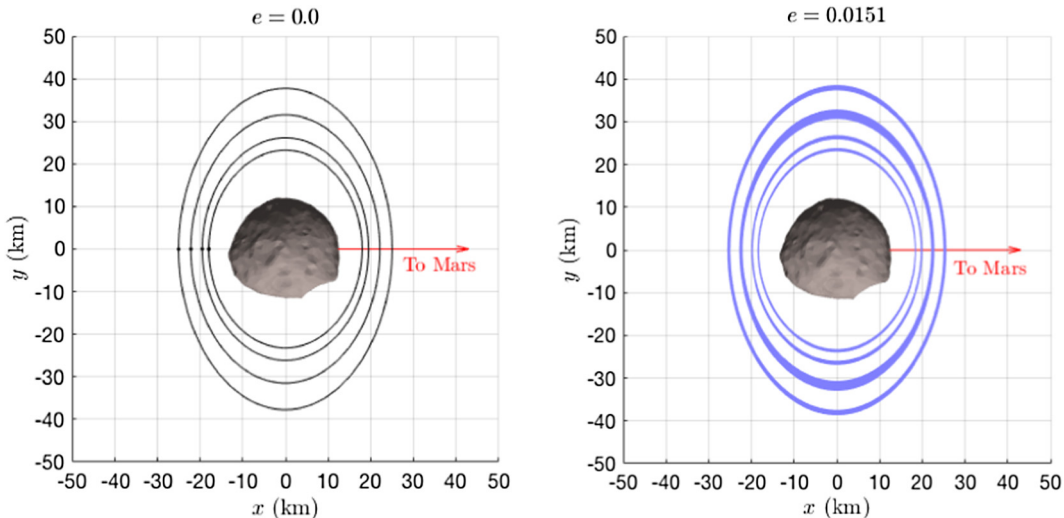


Fig. 16. (a) Family of QSO periodic orbits in the circular Hill problem. (b) Family of quasi-QSO invariant tori in the elliptic Hill problem. The QSO orbits are shown in the synodic Phobos frame, plotted at the stroboscopic time.

4.2.2. Quasi-periodic tori calculation

As pointed out by [Jorba and Villanueva \(1997\)](#), quasi-periodic invariant tori of a six-dimensional non-autonomous Hamiltonian system such as (17) lie in one-parameter families. This is equivalent to periodic orbits in the autonomous circular case. As such, quasi-periodic invariant tori should be seen as key players in understanding and organizing the dynamics of the EHP. In fact, each of the family members of the periodic orbit family illustrated in Fig. 15 is connected to a two-dimensional quasi-periodic orbit (QPO) invariant torus that belong to a more general family of orbits often called “quasi-satellite orbits” (QSO). The current paper does not explore the QSO orbits, but it can be pointed out that they are all fundamentally related to QPO that have in-plane and out-of-plane frequencies, plus forcing frequencies due to the eccentric orbit. Instead, in the current paper a more focused discussion is provided that shows how the planar periodic orbit family bifurcates into a family of QPO as the eccentricity of Phobos is introduced. By showing that these orbits all retain their stability properties, one can establish the link between the QSO and QPO orbits even in the presence of eccentricity. Similarly, these planar QPO families will, when given out-of-plane motions, lie on higher-dimensional tori that have an out-of-plane component. We do not explore this richer set of QPO orbits and leave that analysis for a future work. Instead, in the following we just show that the stable periodic orbits bifurcate into stable QPO when eccentricity is introduced.

These invariant manifolds are computed using the numerical algorithm outlined in [Gómez and Mondelo \(2001\)](#) and [Olikara and Scheeres \(2012\)](#), and summarized in [Baresi et al. \(2018\)](#). The main idea of the algorithm is that quasi-periodic invariant tori can be calculated as invariant curves of a stroboscopic mapping by solving a boundary value problem. The interested reader may find

more information on the methodology in the PhD. thesis of [Olikara \(2016\)](#).

Some example periodic orbits for the circular case are shown in Fig. 16, left while example quasi-periodic orbits for the eccentric case are shown in the right frame. All of the QPOs shown on the right have unity eigenvalues, meaning that they are stable and again are surrounded by families of QPO. This means that perturbations from each of these cases will just oscillate about the nominal solution, again forming the class of QSO motion observed and used for mission design. The quasi-periodic orbits shown on the right are driven by the periodicity of the Phobos eccentric orbit, and one can see that their amplitude grows as they move between the low-order resonances shown in Fig. 15. As the specific resonances are approached, the tori amplitudes shrink until they degenerate into periodic orbits at the precise resonances, meaning that they lose a dimension. The existence of these stable quasi-periodic orbits in the eccentricity driven case imply that precise mission orbit designs can be flown, with consistent periodic crossing of the two distinct periods distributed about the body.

5. Hovering analysis

A final approach to close proximity motion about Phobos is to consider the direct use of thrusting capability to force a spacecraft to “hover” above a given location. An operational analysis of such motion is complex and requires implementation of realistic thruster models, specified relative trajectories, and other details. However, following the approach outlined in [Scheeres \(2012\)](#) and [Broschart and Scheeres \(2007\)](#), the basic stability and implementation of hovering can be analyzed at any given point about a body in terms of the stability structure of an arbitrary equilibrium point, enabled by the addition of constant thrust. Using these published approaches the

basic hovering cost can be identified in terms of total ΔV , the necessary update time to maintain the location within a general criterion, and the dimension of the instability which will have implications for the design of a closed-loop hovering control law.

5.1. Precise computations

Recall the simpler, time-invariant equations of motion relative to Phobos, now incorporating a control acceleration vector $\mathbf{a} = [a_x, a_y, a_z]$.

$$\ddot{x} - 2\omega\dot{y} = 3\omega^2x + U_x + a_x \quad (18)$$

$$\ddot{y} + 2\omega\dot{x} = U_y + a_y \quad (19)$$

$$\ddot{z} = -\omega^2z + U_z + a_z \quad (20)$$

At any given point in the body-relative frame it is possible to provide control accelerations that null out the gravitational and rotational forces so that, given an initially stationary location, the spacecraft will maintain its position in an artificial equilibrium point. The stability of these points can be characterized similarly to a natural equilibrium point (Broschart and Scheeres, 2007). The stability analysis provides a few different insights into the feasibility of hovering at a given location. Almost all hovering locations will be unstable, meaning that there will be hyperbolic manifolds that depart from the ideal hovering location. These directions, and the strength of the time constant, define the direction an ideal hovering spacecraft would drift along and how rapidly it would deviate from the ideal point. Note, this is being evaluated without any assumed closed-loop control, and in fact these values define how a closed-loop control process would have to be designed. The implementation of such hovering need not null out the net forces in a continuous fashion, and more realistically would be implemented using a “dead-band” control approach that leverages the natural dynamics of the system, as outlined in Broschart and Scheeres (2007). Thus, the current analysis just provides a wide overview of the feasibility and needs of a hovering control law.

The key elements of analysis are the total acceleration cost of a hovering location, the stability type of the hovering equilibrium point (which defines the directions and properties of the unstable motion) and the characteristic time of the equilibrium point. The necessary control acceleration is defined as

$$a_x = -(3\omega^2x + U_x) \quad (21)$$

$$a_y = -U_y \quad (22)$$

$$a_z = \omega^2z - U_z \quad (23)$$

with total magnitude $a_T = \sqrt{a_x^2 + a_y^2 + a_z^2}$. Fig. 17 maps the acceleration “cost” of hovering across the planes $x = 0$, $y = 0$, $z = 0$ and $x = y$ in units of mm/s². These can be conveniently transformed into ΔV cost per unit time by multiplying by the desired time unit (e.g., 60 s for 1-min,

3600 s for 1-h, 86,400 for 1-day). Thus, hovering over a region with a cost of 5 mm/s² would require a delta-V cost of 0.3 m/s over one minute, 18 m/s over one hour and 432 m/s over one day. From this it is clear that prolonged hovering requires substantial propellant.

To evaluate the stability characteristics of hovering at an arbitrary point, the linearized equations of motion are stated about the hovering point (treating it as an equilibrium point) and the characteristic equation is formed. Accounting fully for the three-dimensional hovering locations yields a cubic polynomial equation in the eigenvalue squared. The generic form of the linearized equations is

$$\begin{bmatrix} \delta\ddot{x} \\ \delta\ddot{y} \\ \delta\ddot{z} \end{bmatrix} - 2\omega \begin{bmatrix} 0 & 1 & 0 \\ -1 & 0 & 0 \\ 0 & 0 & 0 \end{bmatrix} \begin{bmatrix} \delta\dot{x} \\ \delta\dot{y} \\ \delta\dot{z} \end{bmatrix} = A \begin{bmatrix} \delta x \\ \delta y \\ \delta z \end{bmatrix} \quad (24)$$

$$A = \begin{bmatrix} 3\omega^2 + U_{xx} & U_{xy} & U_{xz} \\ U_{yx} & U_{yy} & U_{yz} \\ U_{zx} & U_{zy} & -\omega^2 + U_{zz} \end{bmatrix} \quad (25)$$

where U_{xy} , etc., is the second partial of the gravitational force potential evaluated at the nominal hovering position. The resulting characteristic equation is then

$$\begin{aligned} & \lambda^6 + \lambda^4[4\omega^2 - \text{Tr}(A)] \\ & - \lambda^2[4\omega^2A_{zz} - (A_{xx}A_{yy} + A_{yy}A_{zz} + A_{zz}A_{xx}) + A_{xy}^2 + A_{yz}^2 + A_{zx}^2] \\ & - \det(A) = 0 \end{aligned} \quad (26)$$

where λ is the characteristic root of the equation. There are several different possible root combinations that can occur generically for such a polynomial. For the current problem (and for the Hill problem in general) only 3 distinct outcomes are found, whose presence can be evaluated using the Routh criterion. These are two negative and one positive real roots (for λ^2), one negative and two positive real roots, and one negative and one complex conjugate pair of roots. The negative roots correspond to oscillatory motion, and can be considered as stable directions, while the positive roots correspond to hyperbolic stable and unstable manifolds and represent instability with a characteristic time $1/\lambda$. The complex roots are similarly unstable with their own characteristic time for the instability. The stability regions are shown in Fig. 18 with the different colors representing one positive root (green), two positive roots (yellow) and complex roots (dark blue). The implication of the different modes of instability are discussed in detail in Broschart and Scheeres (2007), but can be summarized as follows. A single instability can be controlled using a 1-dimensional sensing control loop such as a lidar. On the other hand, in situations with two unstable directions, or a complex instability, the unstable motion will tend to move in a plane requiring additional sensing and control directions. Note that the body is uniformly surrounded by a single instability zone, meaning that for close hovering a stabilizing control that uses a lidar measurement towards the surface can be used. As the hovering alti-

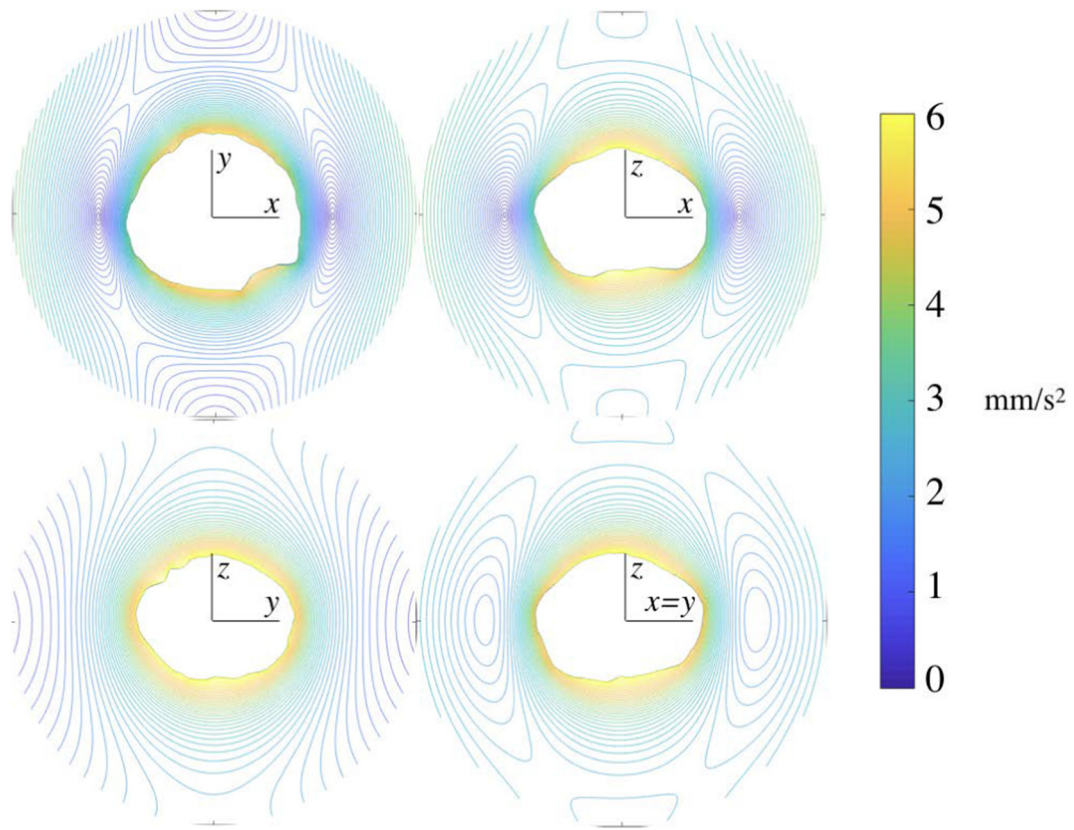


Fig. 17. Hovering cost about Phobos in units of mm/s^2 . Note the zero cost regions about the L_1 and L_2 points.

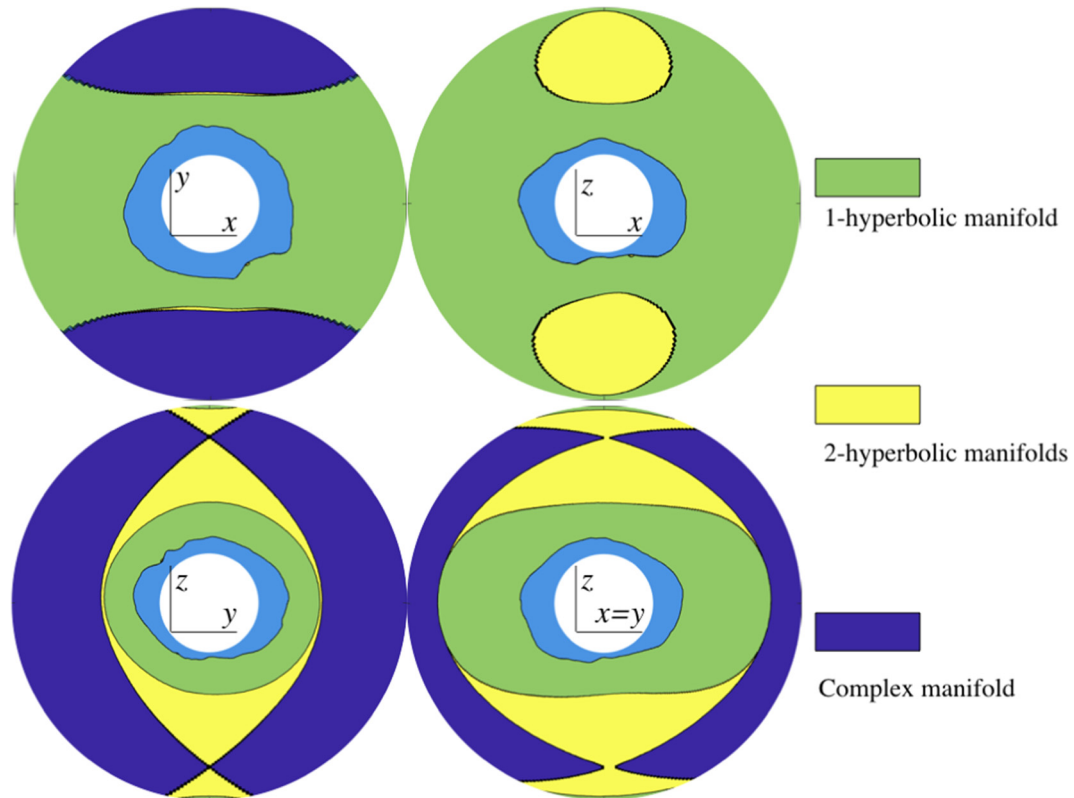


Fig. 18. Stability type in the regions around Phobos. Regions with a single hyperbolic instability can be controlled by a lidar or ranging measurement. Those with multiple hyperbolic or complex instabilities will require lateral sensing and control as well.

tude is increased, the complexity of the environment grows and in the different regimes would require hovering control law implementations that also sense lateral motions.

For each location the value of the eigenvalue is also evaluated, which provides the characteristic time of the instability. For each location the smallest characteristic time (largest exponent) is considered, as this controls the rate at which the satellite will ideally depart from the nominal hovering site, and is a proxy for the frequency with which the control system must sense its state and implement control maneuvers. These are plotted in Fig. 19 in units of h^{-1} , with the maximum values at around 4 per hour when close to the Phobos surface.

5.2. Approximate analysis

It is instructive to validate these results using an approximate model and some simplifying assumptions. Consider hovering above an ideal point mass with the hovering point being placed above the x , y or z axes. This will enable us to better understand the somewhat complex transitions seen for the full model, and show that they are also present even for a simplified gravitational model for Phobos. If one takes the hovering location to be along a single axis at a radius R , with the other dimensions equal to zero, then the matrix A simplifies greatly and has no off-diagonal

terms (i.e., $A_{xy} = A_{yz} = A_{zx} = 0$). The characteristic equation can then be factored by the term $(\lambda^2 - A_{zz})$ and the resulting roots can be found as

$$\lambda_z^2 = A_{zz} \quad (27)$$

$$\lambda_{\pm}^2 = -\frac{1}{2}(4\omega^2 - A_{yy} - A_{xx}) \pm \frac{1}{2} \times \sqrt{(4\omega^2 - A_{yy} - A_{xx})^2 - 4A_{xx}A_{yy}} \quad (28)$$

The second partial of the gravitational force potential μ/r along the transverse axes then equals $-\mu/R^3$, while the second partial evaluated along the hovering direction will equal $2\mu/R^3$. In the following the shorthand notation $n^2 = \mu/R^3$ is used. Consider the three different cases below.

Hovering along x In this case $A_{yy} = -n^2$, $A_{zz} = -(\omega^2 + n^2)$ and $A_{xx} = 3\omega^2 + 2n^2$. Note that $\lambda_z^2 < 0$ and thus is always stable. The two terms in λ_{\pm}^2 are

$$4\omega^2 - A_{yy} - A_{xx} = \omega^2 - n^2$$

As $A_{xx}A_{yy}$ is always negative, the term in the square root will always be larger than $4\omega^2 - A_{yy} - A_{xx}$ and thus there will generally be one positive and one negative root. There will be a degenerate point when $\omega^2 = n^2$, however

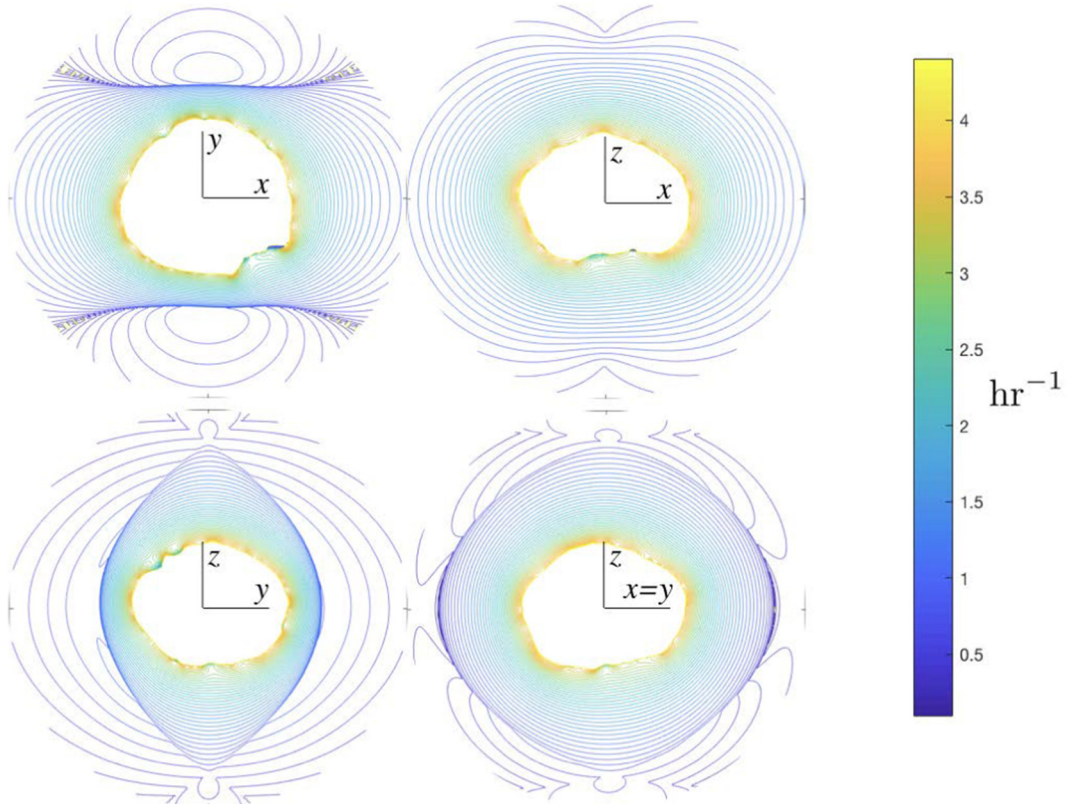


Fig. 19. Largest characteristic exponents of hyperbolic instability in units of h^{-1} . This frequency is a proxy for the relative frequency with which control updates will be required.

the structure of the roots is consistent through this point. Thus, the stability type remains invariant along this axis.

Hovering along y In this case $A_{yy} = 2n^2$, $A_{zz} = -(\omega^2 + n^2)$ and $A_{xx} = 3\omega^2 - n^2$. Note again that $\lambda_z^2 < 0$ and thus is always stable. The two terms in λ_{\pm}^2 are

$$4\omega^2 - A_{yy} - A_{xx} = \omega^2 - n^2 \quad (31)$$

$$A_{xx}A_{yy} = 2n^2(3\omega^2 - n^2) \quad (32)$$

Now the roots take on a more interesting variation as a function of R . For small radii inside of the ideal equilibrium distance $R = (\mu/(3\omega^2))^{1/3}$, $3\omega^2 - n^2 < 0$, meaning that there will be one positive and one negative root. Around the equilibrium distance, however, the $-4A_{xx}A_{yy}$ term will become negative leading to two positive roots. For increasing distance the term in the square root will become more strongly negative eventually leading to a complex root. This is the sequence seen in Fig. 18.

Hovering along z In this case $A_{yy} = -n^2$, $A_{zz} = -\omega^2 + 2n^2$ and $A_{xx} = 3\omega^2 - n^2$. Now note that λ_z^2 will be positive for smaller radius but will eventually go negative once $\omega^2 > 2n^2$. The two terms in λ_{\pm}^2 are

$$4\omega^2 - A_{yy} - A_{xx} = \omega^2 + 2n^2 \quad (33)$$

$$A_{xx}A_{yy} = -n^2(3\omega^2 - n^2) \quad (34)$$

Again the roots take on a more interesting variation as a function of R . For small radii inside of the equilibrium distance $3\omega^2 - n^2 < 0$, meaning that there will be two negative roots for λ_{\pm}^2 , with λ_z^2 being positive and defining the unstable direction. At larger radii one finds $3\omega^2 - n^2 > 0$, creating one negative and positive root for λ_{\pm}^2 , giving the two unstable roots. Finally, at even larger distances $\lambda_z^2 < 0$, leading back to the single unstable root. Again this is the sequence seen in Fig. 18.

6. Conclusion

This paper presents and provides a comprehensive analysis of dynamics about and on the surface of the Martian moon Phobos using the best currently available models. The intent of this paper is to provide support for the planning of missions to this body. We find detailed results for surface motion, including limits on the rate of travel on the surface to ensure contact with the surface. For orbital dynamics, we supply some supplemental results beyond previous research. In particular we map out the families of orbits in the vicinity of the synchronous orbits about Phobos, noting that their bifurcation structure becomes significantly shifted from the ideal symmetric cases most commonly investigated, and we provide detailed analysis and results for the family of stable retrograde orbits about Phobos accounting for the Phobos eccentricity. These orbits retain stability up to contact with the surface and are related to the quasi-satellite orbits that have been studied elsewhere. The paper also details the stability of

hovering motion about Phobos, identifying the basic control needs necessary for implementing such an approach to close proximity motion at this body.

Acknowledgments

The authors acknowledge support from NASA's SSERVI program (Institute for the Science of Exploration Targets) through institute Grant No. NNA14AB03A.

Appendix A. A.1. Phobos constant density gravity field

Following are the Phobos gravity coefficients through order 4 (shown in Table 3). These coefficients are normalized, as defined in Kaula (1966), computed with respect to a normalizing radius $R_s = 11.11881652$ km. The general form of the gravitational field can be expressed as:

$$U = \sum_{l=0}^{\infty} \sum_{m=0}^l \left(\frac{R_s}{r} \right)^{l+1} P_{lm}(\sin \phi) [C_{lm} \cos m\lambda + S_{lm} \sin m\lambda], \quad (35)$$

where P_{lm} are the normalized Legendre polynomials, ϕ is the particle latitude, and λ is the particle longitude in the body-fixed frame.

A.2. Mollweide projection

The Mollweide projection maps any longitude and latitude, (λ, ϕ) respectively, to (x, y) as:

$$\begin{cases} x = \frac{2\sqrt{2}}{\pi} \lambda \cos \theta \\ y = \sqrt{2} \sin \theta \end{cases} \quad \text{with } 2\theta + \sin 2\theta = \pi \sin \phi \quad (36)$$

where one must iteratively solve for ϕ . This projection is advantageous for the visualization of surface distributions since it preserves relative area. Therefore, it avoids the strong distortion near the poles that occurs with a simple

Table 3

Phobos normalized gravity field coefficients through degree and order 4 for a constant density gravity field. A gravity field through degree and order 16 is available from the authors. Definition of the normalization constants can be found in Kaula (1966).

Order l	Degree m	C coefficient C_{lm}	S coefficient S_{lm}
0	0	1.0	–
1	0	0.0	–
1	1	0.0	0.0
2	0	-0.04660347700	–
2	1	0.0	0.0
2	2	0.02418427633	0.0
3	0	0.002998797015	–
3	1	-0.004139321225	0.002045708945
3	2	-0.008785040655	0.001045820499
3	3	0.001185163133	-0.01320053160
4	0	0.006429537912	–
4	1	0.003369680127	-0.001010497508
4	2	-0.002323017571	-0.001589281757
4	3	-0.003114272077	0.002661315051
4	4	0.0008212813403	0.00007342710506

longitude-latitude plot and prohibits accurate visual estimates of the prevalence of regions with a certain value or color. Overlaid on top of the Mollweide plots, we also show lines of constant $\lambda = [-180, -90, 0, +90, +180]$ deg and $\phi = [-60, -30, 0, +30, +60]$ deg.

References

- Baresi, N., Olikara, Z.P., Scheeres, D.J., 2018. Fully numerical methods for continuing families of quasi-periodic invariant tori in astrodynamics. *J. Astronaut. Sci.*, 1–26.
- Broschart, S.B., Scheeres, D.J., 2007. Boundedness of spacecraft hovering under dead-band control in time-invariant systems. *J. Guid. Control Dyn.* 30 (2), 601–610.
- Broucke, R., 1969. Stability of periodic orbits in the elliptic, restricted three-body problem. *AIAA J.* 7 (6), 1003–1009.
- Burmeister, S., Willner, K., Schmidt, V., Oberst, J., 2018. Determination of Phobos' rotational parameters by an inertial frame bundle block adjustment. *J. Geod.*, 1–11.
- Dobrovolskis, A.R., Burns, J.A., 1980. Life near the Roche limit: behavior of ejecta from satellites close to planets. *Icarus* 42 (3), 422–441.
- Gómez, G., Mondelo, J.M., 2001. The dynamics around the collinear equilibrium points of the RTBP. *Phys. D: Nonlinear Phenom.* 157 (4), 283–321.
- Hénon, M., 1969. Numerical exploration of the restricted problem. V. Hill's case: Periodic orbits and their stability. *Acad. Sci. Paris Compt. Rend. Ser. B Sci. Phys.* 268, 223–238.
- Howell, K.C., 1984. Three-dimensional, periodic, 'Halo' orbits. *Celest. Mech.* 32 (January), 73.
- Jorba, A., Villanueva, J., 1997. On the normal behaviour of partially elliptic lower-dimensional tori of hamiltonian systems. *Nonlinearity* 10 (4), 783.
- Kaula, W.M., 1966. Theory of Satellite Geodesy. Applications of Satellites to Geodesy. Blaisdel, Waltham, Mass..
- Kurmaoto, K. MMX science study team, 2016. Origin and evolution of mars to be explored by MMX. In: Proceedings of the 49th ISAS Lunar and Planetary Symposium.
- Marov, M.Ya., Avduevsky, V.S., Akim, E.L., Eneev, T.M., Kremnev, R. S., Kulikov, S.D., Pichkhadze, K.M., Popov, G.A., Rogovsky, G.N., 2004. Phobos-grunt: Russian sample return mission. *Adv. Space Res.* 33 (12), 2276–2280.
- Oberst, J., Zubarev, A., Nadezhina, I., Shishkina, L., Rambaux, N., 2014. The Phobos geodetic control point network and rotation model. *Planet. Space Sci.* 102, 45–50.
- Oberst, J., Willner, K., Wickhusen, K. The DePhine Proposal Team, 2017. DePhine - the deimos and phobos interior explorer - a proposal to ESA's cosmic vision program. In: Proceedings of the 2017 European Planetary Science Congress.
- Olikara, Z., 2016. Computation Of Quasi-Periodic Tori And Heteroclinic Connections In Astrodynamics Using Collocation Techniques PhD thesis. University of Colorado.
- Olikara, Z.P., Scheeres, D.J., 2012. Numerical method for computing quasi-periodic orbits and their stability in the restricted three-body problem. *Adv. Astronaut. Sci.* 145, 911–930.
- Pätzold, M., Andert, T., Jacobson, R., Rosenblatt, P., Dehant, V., 2014. Phobos: observed bulk properties. *Planet. Space Sci.* 102, 86–94.
- Rosenblatt, P., 2011. The origin of the Martian moons revisited. *Astron. Astrophys. Rev.* 19 (1), 44.
- Scheeres, D.J., 1998. The restricted hill four-body problem with applications to the earth-moon-sun system. *Celest. Mech. Dyn. Astron.* 70 (February), 75–98.
- Scheeres, D.J., 2012. Orbital Motion in Strongly Perturbed Environments: Applications to Asteroid, Comet and Planetary Satellite Orbiters. Springer-Praxis, London (UK).
- Scheeres, D.J., Ostro, S.J., Hudson, R.S., Werner, R.A., 1996. Orbits close to asteroid 4769 Castalia. *Icarus* 121 (May), 67–87.
- Scheeres, D.J., Hesar, S.G., Tardivel, S., Hirabayashi, M., Farnocchia, D., McMahon, J.W., Chesley, S.R., Barnouin, O., Binzel, R.P., Bottke, W. F., et al., 2016. The geophysical environment of Bennu. *Icarus* 276, 116–140.
- Van wal, S., Scheeres, D.J., 2016. The lift-off velocity on the surface of an arbitrary body. *Celest. Mech. Dyn. Astron.* 125 (1), 1–31.
- Van wal, S., Scheeres, D.J., 2017. Lift-off velocity on solar-system small bodies. *J. Guid. Control Dyn.*, 1–16.
- Werner, R.A., Scheeres, D.J., 1997. Exterior gravitation of a polyhedron derived and compared with harmonic and mascon gravitation representations of asteroid 4769 Castalia. *Celest. Mech. Dyn. Astron.* 65, 313–344.
- Wiesel, W.E., 1993. Stable orbits about the Martian moons. *J. Guid. Control Dyn.* 16, 434–440.
- Willner, K., Oberst, J., Hussmann, H., Giese, B., Hoffmann, H., Matz, K.-D., Roatsch, T., Duxbury, T., 2010. Phobos control point network, rotation, and shape. *Earth Planet. Sci. Lett.* 294 (3), 541–546.
- Willner, K., Shi, X., Oberst, J., 2014. Phobos' shape and topography models. *Planet. Space Sci.* 102, 51–59.
- Zamaro, M., Biggs, J.D., 2015. Natural motion around the Martian moon Phobos: the dynamical substitutes of the libration point orbits in an elliptic three-body problem with gravity harmonics. *Celest. Mech. Dyn. Astron.* 122 (3), 263–302.
- Zamaro, M., Biggs, J.D., 2016. Identification of new orbits to enable future mission opportunities for the human exploration of the Martian moon Phobos. *Acta Astronaut.* 119, 160–182.